

AEDC-TR-68-251

**ARCHIVE COPY
DO NOT LOAN**

cy1



**EXPERIMENTAL INVESTIGATION OF TWO BLUNT-
TRAILING-EDGE SUPERSONIC COMPRESSOR ROTORS
OF DIFFERENT BLADE THICKNESSES AND WITH
POLYNOMIAL CAMBER LINE**

**C. T. Carman and J. R. Myers
ARO, Inc.
and
A. J. Wennerstrom
Aerospace Research Laboratories**

January 1969

This document has been approved for public release
and sale; its distribution is unlimited.

**ENGINEERING SUPPORT FACILITY
ARNOLD ENGINEERING DEVELOPMENT CENTER
AIR FORCE SYSTEMS COMMAND
ARNOLD AIR FORCE STATION, TENNESSEE**

AEDC TECHNICAL LIBRARY



5 0720 00031 8529

PROPERTY OF U. S. AIR FORCE
AEDC LIBRARY
F40600 - 69 - C - 0001

NOTICES

When U. S. Government drawings specifications, or other data are used for any purpose other than a definitely related Government procurement operation, the Government thereby incurs no responsibility nor any obligation whatsoever, and the fact that the Government may have formulated, furnished, or in any way supplied the said drawings, specifications, or other data, is not to be regarded by implication or otherwise, or in any manner licensing the holder or any other person or corporation, or conveying any rights or permission to manufacture, use, or sell any patented invention that may in any way be related thereto.

Qualified users may obtain copies of this report from the Defense Documentation Center.

References to named commercial products in this report are not to be considered in any sense as an endorsement of the product by the United States Air Force or the Government.

EXPERIMENTAL INVESTIGATION OF TWO BLUNT-
TRAILING-EDGE SUPERSONIC COMPRESSOR ROTORS
OF DIFFERENT BLADE THICKNESSES AND WITH
POLYNOMINAL CAMBER LINE

C. T. Carman and J. R. Myers

ARO, Inc.

and

A. J. Wennerstrom

Aerospace Research Laboratories

This document has been approved for public release
and sale; its distribution is unlimited.

FOREWORD

This report was prepared by Charles T. Carman and J. R. Myers of ARO, Inc. (a subsidiary of Sverdrup & Parcel and Associates, Inc.), contract operator of the Arnold Engineering Development Center (AEDC), Air Force Systems Command (AFSC), Arnold Air Force Station, Tennessee, and Dr. Arthur J. Wennerstrom and 1st Lt John W. Steurer of the Fluid Dynamics Facilities Research Laboratory of the Aerospace Research Laboratories, Office of Aerospace Research (OAR), Wright-Patterson Air Force Base, Ohio. Mr. J. Salvage, candidate for a Masters Degree at the University of Tennessee Space Institute, assisted greatly in the reduction and analysis of data.

This is the second of a series of reports which presents detailed experimental data from a supersonic compressor research program. Aerodynamic design of the compressor rotors was conducted at the Aerospace Research Laboratories. Mechanical design and experimental work were conducted at AEDC. The complete program was sponsored by the Aerospace Research Laboratories under Program Element 614450F, "Aerospace Simulation Techniques Research," under the direction of Mr. Elmer G. Johnson.

The work was performed under ARO Project No. TW5702 between January and May 1967, and the manuscript was submitted for publication on October 10, 1968.

This technical report has been reviewed and is approved.

Hans K. Doetsch
Technical Advisor
Research Division
Directorate of Plans
and Technology

Edward R. Feicht
Colonel, USAF
Director of Plans
and Technology

ABSTRACT

Two configurations of blunt-trailing-edge supersonic compressor blades incorporating a polynomial camber line were tested with air in the AEDC compressor rig. The performance of these blades was investigated over the speed range from 50 to 100 percent of design speed. The performance of the two blade configurations is compared, and the effect of the modifications between the two configurations is evaluated. A comparison of selected performance data obtained with circular arc blading tested previously and the polynomial camber blading is made to evaluate the effects of the camber redistribution.

CONTENTS

	<u>Page</u>
ABSTRACT	iii
NOMENCLATURE	vii
I. INTRODUCTION	1
II. BLADE-ELEMENT DESIGN	2
III. COMPRESSOR DESIGN	6
IV. APPARATUS	8
V. PROCEDURE	9
VI. RESULTS AND DISCUSSION	9
VII. CONCLUSIONS	12
REFERENCES	13

APPENDIXES

I. ILLUSTRATIONS

Figure

1. Second Derivative of the Mean Chord Line	17
2. Leading-Edge Profile	17
3. Compressor Rotor No. 2	18
4. Cascade Geometry	20
5. Cross-Sectional View of Experimental Compressor	21
6. Details of Instrumentation Stations	22
7. Comparison of Rotor Efficiencies, R2C1 and R2C2	25
8. Comparison of Rotor Total Pressure Ratio, R2C1 and R2C2	25
9. Comparison of Static Pressure Axial Profiles, 100-percent Speed, R2C1 and R2C2	26
10. Efficiency Distribution at Design Speed and Maximum Back Pressure, R2C1 and R2C2	27
11. Total Pressure Distribution at Design Speed and Maximum Back Pressure, R2C1 and R2C2	27
12. Corrected Enthalpy Rise at Design Speed and Maximum Back Pressure, R2C1 and R2C2	27

<u>Figure</u>	<u>Page</u>
13. Absolute Exit Mach Number Distribution at Design Speed and Maximum Back Pressure, R2C1 and R2C2	28
14. Absolute Exit Angle Distribution at Design Speed and Maximum Back Pressure, R2C1 and R2C2	28
15. Specific Mass Flow Distribution at Design Speed and Maximum Back Pressure, R2C1 and R2C2	28
16. Comparison of Rotor Efficiencies, R1C1 and R2C2	29
17. Comparison of Rotor Total Pressure Ratio, R1C1 and R2C2	29
18. Comparison of Static Pressure Axial Profiles, 100 Percent Speed, R1C1 and R2C2	30
19. Efficiency Distribution at Design Speed and Maximum Back Pressure, R1C1 and R2C2	31
20. Total Pressure Distribution at Design Speed and Maximum Back Pressure, R1C1 and R2C2	31
21. Absolute Flow Angle at Design Speed and Maximum Back Pressure, R1C1 and R2C2	32
22. Corrected Exit Specific Mass Flow at Design Speed and Maximum Back Pressure, R1C1 and R2C2	32
 II. TABLES	
I. Midradius Rotor Blade Coordinates for R2C1	33
II. Midradius Rotor Blade Coordinates for R2C2	34
III. MEASUREMENT UNCERTAINTY	35
IV. METHODS OF CALCULATION	40
V. DATA SUMMARY FOR CONFIGURATIONS R2C1 and R2C2	43

NOMENCLATURE

A	Area, in. ²
a, b	Constants
C	Absolute velocity, ft/sec
C _f	Flow coefficient
C _p	Specific heat at constant pressure
c	Chord length
d	Axial distance from blade leading edge, in.
F	Weight flow, lb/sec
G	Specific weight flow, lb/sec-in. ²
g	Local acceleration of gravity, 32.14 ft/sec ²
H	Enthalpy, passage height
IW	Inner wall of compressor annulus
J	Mechanical equivalent of heat, 778.3 ft-lb/Btu
k	Maximum value of y'' (Eq. (1))
M	Mach number
N	Rotational speed, rpm
OW	Outer wall of compressor annulus
P	Total pressure, psia
p	Static pressure, psia
R	Gas constant for air, 53.34 ft-lb/lb°R
Re	Reynolds number
RF	Thermocouple impact-recovery factor
RP	Pressure ratio
r	Radius, in.
s	Blade spacing, in.
T	Total temperature, °R
t	Static temperature, °R and thickness, in.

U	Circumferential blade velocity, ft/sec
W	Relative velocity, ft/sec
w	Passage width between blades
x, y	Coordinates
y', y''	Chord-line derivatives
α	Absolute flow angle relative to axis of rotation, deg
β	Relative flow angle, deg
γ	Ratio of specific heats
δ	Ratio of inlet total pressure to the ARDC model sea-level atmosphere (14.7 psia)
η	Adiabatic efficiency
θ	Ratio of inlet absolute total temperature to absolute total temperature of ARDC model sea-level atmosphere (519.3°R)
λ	Constant

SUBSCRIPTS

0, 1, 2, 3	Compressor instrumentation stations
a	Adiabatic
av	Average
calc	Calculated
deg	Degrees
i	Indicated
isen	Isentropic
m	Maximum
w	Relative

SECTION I INTRODUCTION

Investigations of supersonic axial-flow compressors (i. e., compressors having supersonic velocities relative to the blade row) have most commonly employed either of two design approaches. One has been to limit diffusion in the rotor to generally accepted values, thereby placing the burden of the problem on the stator. The other has been to strive for very high diffusion in the rotor, permitting the stator to operate at conventional diffusion levels. The supersonic compressor research program of the Aerospace Research Laboratories is attempting to achieve very high diffusion in the rotor. To date, the program has only considered rotors of relatively high solidity which employ blades having blunt trailing edges; i. e., the maximum blade thickness is at 100-percent chord. This design concept was first proposed in Ref. 1. The blading is designed such that the flow passages have relatively constant area and, as a result of camber, the trailing edges remain blunt. The annulus is not converged. The geometry is arranged with a suitable passage length-to-width ratio such that a pseudo-shock diffusion is encouraged between blades. The flow at the trailing edges is allowed to undergo a sudden-area-increase diffusion process which is reasonably efficient if the trailing-edge Mach number is not close to unity. A complete discussion of the design philosophy is given in Ref. 2.

The overall performance of the first configuration tested was discussed and compared with a theoretical analysis in Ref. 3. This configuration employed a circular-arc camber distribution and a rotor passage divergence of approximately 10 percent. In general, the performance was poor. However, the theoretical analysis suggested that this performance could be improved by incorporating the following modifications: (1) a reduction in the blade trailing-edge thickness, (2) a redistribution of the blade camber, and (3) annulus contouring.

The first report in this series (Ref. 4) dealt with the effects of reducing the blade trailing-edge thickness. The blade surfaces of midradius were circular arcs extending from a small leading-edge radius to a point of maximum thickness at the trailing edge. It was concluded that the configuration tested demanded too much diffusion for the rotor or the downstream diffusion zone to handle efficiently. Separation was believed to have occurred in the rotor passage and on the outer wall of the annulus. Reducing the blade trailing-edge thickness, which as a consequence increases the amount of divergence in passage area occurring through the blade row, did not lead to an increase in performance. It appeared that opening the blade passage served only to move the free surface of the fluid

a corresponding amount further away from the suction surface of each blade. The fluid mainstream remained virtually unchanged.

Complete data from two rotors are presented in this report. Both rotors employ blade surfaces symmetrical about a camber line which is generated by a fourth-order polynomial. The camber distribution incorporates essentially zero curvature in the leading portion of the blade. The two rotors described herein differ only in the blade thickness at the trailing edge and, as a consequence, in the amount of divergence in passage area which occurs through the blade row. All other characteristics are identical. Comparison of selected data from these rotors was made in an effort to confirm the previous conclusions regarding the effects of reducing the blade trailing-edge thickness. In addition, a comparison of selected performance data of the circular-arc blading and the fourth-order polynomial blading was made to evaluate the effects of the camber redistribution.

SECTION II BLADE-ELEMENT DESIGN

2.1 GENERAL CONSIDERATIONS

The rotor configurations described in this report were designed to provide a more favorable camber distribution than the circular-arc distribution previously reported in Ref. 4. This was accomplished by imposing certain related restrictions upon the blade surface contours. The first of these was to require that the leading portion of the compressor airfoil have little or no curvature. Maximum curvature, therefore, occurs well to the rear. The effect of this is primarily to minimize the supersonic expansion which takes place on the suction surface upstream of the first passage shock waves. Locating maximum curvature to the rear of the blade ensured that most of the turning and associated high losses would take place at the lowest passage Mach number. The second restriction was to require that the airfoil curvature be continuous between the leading and trailing edges. This means that no discontinuities existed in either the first or second derivative of the equation defining the camber line coordinates. Neither were any discontinuities permitted to exist in the first or second derivatives of the equation defining the coordinates of the airfoil surface, with exception of the transition zones at the leading and trailing edges. Continuous curvature was required to minimize the tendency for the fluid boundary layers to separate from the airfoil surface. The third restriction was that maximum airfoil camber occur downstream of the midchord position

but not necessarily coincide with the peak value of the chord-line second derivative. At the trailing edge, a value of the camber line second derivative less than its maximum was chosen to give the flow slightly better guidance leaving the rotor than it would obtain if this maximum occurred at the trailing edge.

2.2 DEVELOPMENT OF BLADE-ELEMENT SHAPE

To satisfy the above constraints, the chord line chosen prescribed a parabolic distribution for the second derivative of the mean line, progressing from zero at the leading edge to a maximum aft of midchord, then decreasing to some fraction of the maximum value. This is described by Eq. (1) and illustrated in Fig. 1 (Appendix I), where y'' and k have negative values. The airfoil chord-line coordinates are considered in an x - y plane with x corresponding to the axial direction and y to the tangential direction. x varied from 0 at the leading edge to 1 at the trailing edge. The equation of the parabolic distribution of y''_m is

$$(x - h)^2 = 4a(y''_m - k) \quad (1)$$

where h is the location of the maximum value of the chord-line second derivative y''_m , k is the (numerically) maximum value of y'' , and a is a constant. The condition that $y''_m = 0$ at $x = 0$ leads to

$$k = -h^2/4a \quad (2)$$

Solving Eq. (1) for y''_m and introducing Eq. (2) gives

$$y''_m = \frac{1}{4a} x^2 - \frac{h}{2a} x \quad (3)$$

Integrating Eq. (3) once gives the chord-line tangent distribution,

$$y'_m = \frac{1}{12a} x^3 - \frac{h}{4a} x^2 + b \quad (4)$$

where b is the constant of integration. A second integration leads to

$$y_m = \frac{1}{48a} x^4 - \frac{h}{12a} x^3 + bx \quad (5)$$

which defines the actual coordinates of the chord line. The constant of integration normally appearing in Eq. (5) has been set equal to zero, which places the leading edge of the airfoil at $x = 0$, $y = 0$.

Constants a , b , and h must be established in order to fully define the curve. The three conditions defining these constants are:

1. inlet tangent to chord line, $= \tan \gamma_1$ at $x = 0$,
2. outlet tangent to chord line, $= \tan \gamma_2$ at $x = 1$,
3. ratio of outlet y'_m to maximum $y'_m = \lambda$ at $x = 1$.

The first condition applied to Eq. (4) gives directly

$$b = \tan \gamma_1 \quad (6)$$

The second condition applied to Eq. (4) leads to

$$\tan \gamma_2 = -\frac{1}{12a} - \frac{h}{4a} + \tan \gamma_1$$

or, after rearrangement,

$$a = \frac{3h - 1}{12(\tan \gamma_1 - \tan \gamma_2)} \quad (7)$$

The third condition inserted into Eq. (1) leads to

$$(1 - h)^2 = 4ak(\lambda - 1)$$

Combining this with Eq. (2) gives an equation quadratic in h ,

$$\lambda h^2 - 2h - 1 = 0$$

having the solution

$$h = \frac{1}{\lambda} (1 - \sqrt{1 - \lambda}) \quad (8)$$

Now that the chord line is defined, a thickness distribution must be applied. The thickness distribution chosen for the present investigation is the blunt-trailing-edge type which arises from specifying a flow passage of essentially constant area. A small, smooth increase in passage area is desirable between leading and trailing edge in order to compensate for boundary-layer growth. Also, a finite but small leading-edge radius is desirable for manufacturing and heat-transfer considerations. Sufficient thickness must be provided near the leading edge for mechanical strength. These conditions led to selection of a two-step procedure defining the thickness distribution.

The leading edge must be fine, the airfoil must smoothly increase in thickness, and there should be a minimum discontinuity in the first or second derivatives of the airfoil surface where the leading-edge portion joins the after portion. A secant curve satisfies this requirement, having a somewhat parabolic shape but having extremities which become asymptotically parallel. A leading-edge contour having the geometry shown in Fig. 2 was selected for the overall airfoil shown in Fig. 3 with $\alpha = 0.1$, $\beta = 0.6$, $r = 0.02$, and $\theta \approx 60$ deg. The leading-edge contour in x^* , y^* -coordinates is defined

$$x^* = \frac{1}{P} \sec^{-1} \left(\frac{y^*}{N} + 1 \right) \quad (9)$$

Negative values of x^* apply to the suction surface and positive to the pressure surface. The variable y^* is also directly

$$y^* = x \sec \theta \quad (10)$$

This leading-edge contour is to be applied to the camber line between $x = 0$ and $x = \alpha$ and to be tangent to a circle of radius r with center on the camber line at $x = \alpha$. The transfer from the x^* , y^* -coordinate system to the x , y -coordinates of the airfoil surface is possible with

$$x = x_m + x^* \sin \theta \quad (11)$$

$$y = y_m - x^* \cos \theta \quad (12)$$

As the product Px^* goes to $\pi/2$, y^* approaches infinity. A leading edge of reasonable sharpness requires that Px^* have some value less than $\pi/2$ at $x = \alpha$. Leading-edge boundary conditions at $x = \alpha$ may be defined

$$x^* = \pm r$$

$$\sec^{-2} \left(\frac{y^*}{N} + 1 \right) = \pm \frac{\beta\pi}{2}$$

which give for the constants of Eq. (9)

$$N = \frac{\alpha \sec \theta}{\left(\sec \frac{\beta\pi}{2} - 1 \right)} \quad (13)$$

$$P = \frac{\beta\pi}{2r} \quad (14)$$

For the best match of leading-edge surface contour to afterbody contour, θ should be calculated from the equation

$$\theta = \tan^{-1} \frac{y_m}{\alpha} \quad (15)$$

where y_m is the value computed with Eq. (5) for $x = \alpha$.

The airfoil thickness downstream of $x = \alpha$ shall be distributed in such a manner that the flow passage between blade increases in area by the fraction w between $x = \alpha$ and $x = 1$. This is chosen to compensate for boundary-layer development. The passage area shall be assumed to proceed linearly with x . Airfoil thickness at α , in the y -direction, may be defined

$$t = 2r\sqrt{1 + (y'_m)^2}$$

The effective passage width between blades is

$$w = \frac{s - t}{\sqrt{1 + (y'_m)^2}}$$

Passage height shall be defined as H and is not restricted to a constant. The passage area ratio between $x = \alpha$ and any point downstream may be written

$$\frac{A}{A_a'} = \frac{H \frac{s-t}{\sqrt{1+(y'_m)^2}}}{\left\{ H \frac{s-t}{\sqrt{1+(y'_m)^2}} \right\}_{x=a}} = 1 + w \left(\frac{x-a}{1-a} \right) \quad (16)$$

Rearranging, the equation for airfoil thickness is

$$t = s - \frac{\sqrt{1+(y'_m)^2}}{H} \left[1 + w \left(\frac{x-a}{1-a} \right) \right] \left[H \frac{s-t}{\sqrt{1+(y'_m)^2}} \right]_{x=a} \quad (17)$$

The y-coordinates of the airfoil surfaces are obtained by

$$\begin{aligned} y &= y_m + t/2 \text{ (suction surface)} \\ y &= y_m - t/2 \text{ (pressure surface)} \end{aligned} \quad (18)$$

The tangential spacing, s , between airfoils is obtained by specifying the desired solidity, c/s , and calculating the chord length. Chord length is defined by

$$c = \sqrt{1 + y_m^2} \quad (19)$$

where y_m is the terminal value of y_m computed with Eq. (5).

SECTION III COMPRESSOR DESIGN

With the exception of blade-element shape, the rotors tested in this report were aerodynamically similar to those reported in Ref. 4. The blunt-trailing-edge concept was retained. As before, a midradius inlet blade angle of 60 deg (from axial) and a midradius exit blade angle of 30 deg were employed, resulting in a camber of 30 deg. To provide a high passage length-to-width ratio with which to encourage a pseudo-shock diffusion process, the solidity of 3.0 was retained. The mean radius relative inlet Mach number at design speed and zero incidence would be 1.7.

The blade-element shape was prescribed by the method described in the preceding section. Since no hub or tip contouring was employed for the configurations presented in this report, the passage height, H , was set equal to a constant. The trailing-edge value of the second derivative of the chord line, y''_m , was set equal to half its maximum value ($\lambda = 0.5$). Values of $r = 0.02$, $\beta = 0.6$, and $\alpha = 0.1$ (see Fig. 2) were used to define the leading portion of both configurations tested.

The hub/tip radius ratio for these tests was 0.9, and the rotor tip diameter was 22 in.

Because of the high solidity and relatively short chord length, a large number (126) of blades resulted. Since blade attachment would have been excessively expensive, the blading was machined directly into the rim of the wheel. The blade surfaces between hub and tip were generated by a line passing through, and normal to, both the compressor axis and the outline of the specified midradius blade-element. As a result, the blades are slightly thicker at the tip than at the root.

The first configuration tested is shown in Fig. 3a. The geometry at midradius was as illustrated in Fig. 4 with $t_2 = 0.2390$ in. and $s = 0.5258$ in. A parameter which has proven useful for performance calculations with blunt-trailing-edge blades (see Ref. 3) is the ratio of trailing-edge thickness to blade spacing, measured circumferentially. The thickness-to-spacing ratio for this first configuration was 0.455. This value results from specifying a passage area divergence of 10 percent from entrance to exit. The same relative passage divergence existed for the circular-arc blading reported in Ref. 4. However, the method used to determine the passage divergence for the circular-arc blading was based upon the ratio of cross sections normal to the relative flow, defined as follows. The inlet section extended from the leading-edge pressure surface of one blade normal to the suction surface of the adjacent blade. The outlet section extended from the trailing-edge suction surface of one blade normal to the pressure surface of the adjacent blade. This is not the same method as described in Section II of this report. Therefore, comparison of the amount of divergence between blades shapes is only approximate.

The geometry of the second configuration at midradius differs from the first only in that the thickness-to-spacing ratio was reduced to 0.395 by removing material from the blades as shown in Fig. 3b. This corresponds to a passage area increase of approximately 22 percent. All other characteristics are identical. The value of 0.395 was chosen in order to enable comparison with data from circular-arc blading of the same value.

The coordinates of the blade surfaces at midradius are given in Tables I and II (Appendix II).

SECTION IV APPARATUS

4.1 COMPRESSOR RIG

Since complete details on the compressor rig are presented in Ref. 5, only a limited description is provided here. A cross section of the compressor is shown in Fig. 5. The incoming air is drawn from a large settling chamber containing a straightener and screens. The inner wall of the outer casing is completely cylindrical throughout the entire central section of the compressor, and the hub wall is also cylindrical downstream of the compressor. However, the base of the bulletnose which extends into the central section of the compressor is a 1.0-deg cone to provide a slight flow acceleration all the way to the rotor leading-edge plane. The discharging flow enters a radial diffusing section which terminates in a circumferential throttle valve. The throttle valve has a series of equally spaced and sized discharge ports around the periphery to eliminate as much as possible any asymmetric conditions which might feed back to the compressor. No stator blade rows were used in conjunction with these experiments. The test rig is a closed-loop system, incorporating a heat exchanger in the return loop and a venturi to measure mass flow. Inlet total pressure and temperature were maintained at approximately standard atmospheric conditions, and all presented data are corrected to standard conditions.

4.2 INSTRUMENTATION

Aerodynamic pressures and/or temperatures are measured at the stations shown in Fig. 5. Axial and radial locations and details of the measuring stations in the compressor and venturi are shown in Fig. 6.

Total pressure and total temperature upstream of the rotor were measured with pairs of 5-element rakes placed 1.0 in. ahead of the rotor. These pressure probes were simple impact tubes since the flow direction is uniform and known. The temperature probes contain iron-constantan thermocouples in diffuser shrouds. The probe elements were centered at the centroids of circumferential bands of equal flow area. Total pressure and total temperature downstream of the rotor were each measured with a pair of 5-element rakes placed 2.0 in. behind the rotor. These were similar to the upstream rakes, except that the pressure probes were of the directionally insensitive Kiel design. Radial traverses were made to measure total pressure and flow angle at locations 0.5 and 2.0 in. behind the rotor. Two- and three-hole prism-type yaw

probes were used for measuring flow angle and flow angle plus total pressure. A row of static pressure taps of 0.025-in. diameter were located in the outer casing beginning upstream, across, and downstream of the rotor. Additional static taps were placed at corresponding locations on the hub wall, up and downstream of the rotor.

The aerodynamic pressure data were measured with strain-gage transducers, and temperatures were measured with thermocouples. The outputs from these instruments are processed through an analog-to-digital converter and recording system. This system completed a scan of 100 channels in one minute.

The measurement uncertainty is discussed in Appendix III, and the methods of calculations are given in Appendix IV.

SECTION V PROCEDURE

The compressor rotors were tested between 50- and 100-percent design speed in increments of 10-percent speed. Design corrected tip speed was 1600 ft/sec. Performance data were measured at each speed from choked flow (wide open throttle) to audible surge. Three complete data scans were recorded at each test point, and the average values were used in the data reduction process. The yaw probes were traversed once during each test point.

SECTION VI RESULTS AND DISCUSSION

6.1 GENERAL ROTOR PERFORMANCE

6.1.1 Rotor No. 2, Configuration No. 1

Complete experimental data for this configuration are presented in Appendix V, Table V-I. Maximum design-speed pressure ratio was 2.25, at which point the adiabatic efficiency was 61.5 percent. Peak efficiency continuously increased as speed was reduced, reaching 76 percent at 50-percent speed. The relative inlet Mach number at design speed, and maximum pressure ratio, varied from 1.44 at the hub to about 1.55 at the tip.

As observed with the circular-arc blading, separation occurs on the outer casing wall immediately downstream of the rotor at 90- and 100-percent speeds. This is evidenced by radial traverse data taken 0.75-in. downstream of the rotor exit plane. Again, too much diffusion is demanded in the rotor passageway, causing the development of thick boundary layers. Upon leaving the rotor, this low energy flow is unable to overcome the diffusion zone pressure gradient and separates from the annulus casing.

6.1.2 Rotor No. 2, Configuration No. 2

Complete experimental data for this configuration are presented in Appendix V, Table V-II. Maximum design-speed pressure ratio was 2.28, at which point the adiabatic efficiency was 60.5 percent. Peak efficiency continuously increased as speed was reduced, reaching 81 percent at 50-percent speed. The relative inlet Mach number at design speed, and maximum pressure ratio, varied from 1.47 at the hub to about 1.59 at the tip.

The radial traverse data and static pressure distribution are similar to those of Configuration 1. The general remarks of the preceding section regarding separation also pertain to this rotor.

6.2 COMPARISON OF ROTOR PERFORMANCE

6.2.1 Effect of Reducing the Trailing-Edge Thickness

The compressor maps of Configurations 1 and 2 are superimposed in Figs. 7 and 8 for 60-, 80-, and 100-percent speeds. Little difference exists in the design speed performance of the two rotors. A similar result was observed for the circular-arc blading discussed in Ref. 4. It follows that for both the circular-arc configuration and the present configuration, the increase in passage area is accompanied by a nearly proportional increase in flow blockage with no increase in performance.

The low speed performance of Configuration 2 is slightly higher than that of Configuration 1. An increase in flow is also evident. This is logical since the effects of boundary-layer blockage and flow separation decrease with decreasing back pressure and rotor speed.

The annulus wall static pressure distribution and the radial distributions of various parameters are superimposed and presented in Figs. 9

through 15. The increase in static pressure level of Configuration 2 most likely reflects a change in the radial distribution of the flow rather than increased diffusion in the rotor passageway. The dip in static pressure distribution just downstream of the rotor exit is attributed to a local separation zone. A similar distribution was evident for the circular-arc configuration (see Ref. 3). Only slight differences in performance are evident from comparison of the radial distributions.

6.2.2 Effect of Redistributing the Blade Camber

In this section selected data are compared for two rotors having the same thickness-to-spacing ratio but different camber distributions. Rotor No. 1, Configuration 1 (R1C1) has a circular-arc mean camber-line distribution. Complete data for this configuration are given in Ref. 4. Rotor No. 2, Configuration 2 (R2C2) was discussed in Section 6.1.2.

It can be seen from the superposed compressor maps, Figs. 16 and 17, that R1C1 chokes at a higher value of mass flow than R2C2 at low speeds; however, this difference diminishes with increasing speed and reverses above 90-percent speed. The difference in choking flow at low speeds can be attributed directly to a difference in throat area between the two configurations. R1C1 has a ratio of minimum passage width to blade spacing of 0.47 at midradius. The upstream relative flow angle corresponding to this condition is $\cos^{-1} 0.47$ or 62 deg. This compares well with 61.8 deg measured at midradius with 60-percent speed, at which condition the relative inlet Mach number is nearly 1.0. R2C2 has a minimum passage width-to-blade spacing ratio of 0.44. This corresponds to an inlet angle of 63.9 deg, which is very close to the 63.7-deg value measured at 60-percent speed with R2C2.

As relative inlet Mach number increases, the choking incidence becomes less affected by throat area and is controlled by other criteria which are not so simply defined. The higher flow measured at 100-percent speed with R2C2 is quite likely attributable to the sharper leading edges, and possibly also the reduced inlet camber, employed with this configuration. No means of predicting choking incidence at the higher speeds is offered at this time. Both configurations operated at a midradius relative inlet angle of approximately 67.5 deg (7.5-deg incidence) at 100-percent speed.

The stalling pressure ratio of R2C2 was marginally lower (about 2 or 3 percent) than that of R1C1 at all speeds. The peak efficiencies of

R2C2 were higher by about the same amount. The efficiency improvement is attributed to a more efficient blade element pressure distribution and a lower inlet suction-surface expansion existing with R2C2. The reduced inlet expansion is quite evident from the wall static pressure distributions in Fig. 18. The slight decrease in pressure ratio is attributed to a larger deviation angle which is likely to exist with R2C2 because of the concentration of camber to the rear of the blade. Deviation angles were not calculated because of the necessity of correcting measured values for the changes occurring in the rotor wake area. The ability to accomplish this accurately was considered doubtful.

Stalling values of mass flow were approximately the same for both rotors. The change in blade contour did not appear to have any appreciable effect on limiting diffusion. This seemed to depend primarily on the trailing-edge blockage, which was approximately the same value for both configurations. Thus the flow range between stall and choke was smaller with R2C2 than R1C1 at lower speeds because of the difference in choking flow rates.

R2C2 produced a significantly higher static pressure rise on the outer casing than R1C1, with most of the increase occurring in the wake area immediately downstream of the rotor. From examination of the radial distributions of efficiency and total pressure ratio measured two inches downstream of the rotor, Figs. 19 and 20, it appears that the higher casing static pressure at that location is a direct result of a higher total pressure in the outer zone. This, in turn, is caused by lower losses, evident through higher efficiency, in this zone. The ratio of the outermost total pressure ratios shown for the two configurations in Fig. 20 is approximately equal to the ratio of the static pressures two inches downstream shown in Fig. 18. Since the flow angles are approximately equal (Fig. 21), the absolute Mach numbers are approximately equal at the outer casing. The blade contour of R2C2 appears to produce a more uniform discharge flow than that of R1C1 (Fig. 22); however, it is far from ideal.

SECTION VII CONCLUSIONS

It was concluded that the redistribution of camber from the circular-arc profile to the fourth-order polynomial profile had little effect on the overall performance of the rotor. Diffusion was excessive, flow separation resulted, and the performance of the rotor was poor. However, the modified contour did reduce the leading-edge

expansion which undoubtedly contributed to the slight increase in efficiency recorded at design speed.

Two blades of similar shape but different thickness-to-spacing ratio were also compared in this report. The results are consistent with the conclusions reached in Ref. 4 for the circular-arc blading; i. e., increasing passage divergence does not lead to an increase in performance. It appears that opening of the blade passage results in a proportional increase in the size of the separation zone. The main-stream is unaffected, and therefore performance remains substantially the same.

The four configurations discussed to date have not employed annulus convergence and, as a result, blade loading is very high, particularly in the tip region. Under these conditions, the flow separates. The gross separation is of such magnitude that exceptionally large mixing losses occur in the rotor discharge region. These losses, which are nearly equal for all the configurations reported, dominate the performance. The following effort will be aimed at reducing and redistributing the blade loading through annulus modification to R1C2. A later experiment will consider a more favorable rotor twist distribution.

REFERENCES

1. Johnson, E. G., von Ohain, H., Lawson, M. D., and Cramer, K. R. "A Blunt-Trailing Edge Supersonic Compressor Blading." WADC-TN-59-269, 1959.
2. Chauvin, J. "The Concept of Blunt-Trailing-Edge Blading for Use in Supersonic Compressors." Paper DK 533-697-242-011.5 Jahrbuch 1962 der WGLR, Vieweg and Sohn, Braunschweig, Germany, 1963.
3. Wennerstrom, A. J. and Olympios, S. "A Theoretical Analysis of the Blunt-Trailing-Edge Supersonic Compressor and Comparison with Experiment." ARL 66-0236, 1966.
4. Carman, C. T., Myers, J. R., Steurer, J. W., and Wennerstrom, A. J. "An Experimental Investigation of Two Blunt-Trailing-Edge Supersonic Rotors of Different Thickness; Circular-Arc Camber Line." AEDC-TR-68-197 (AD), 1968.
5. Carman, C. T. "Development of the Supersonic Compressor Test Facilities at the Arnold Engineering Development Center." AEDC-TR-65-169 (AD471021), 1965.

APPENDIXES

- I. ILLUSTRATIONS**
- II. TABLES**
- III. MEASUREMENT UNCERTAINTY**
- IV. METHODS OF CALCULATION**
- V. DATA SUMMARY FOR CONFIGURATIONS R2C1 AND R2C2**

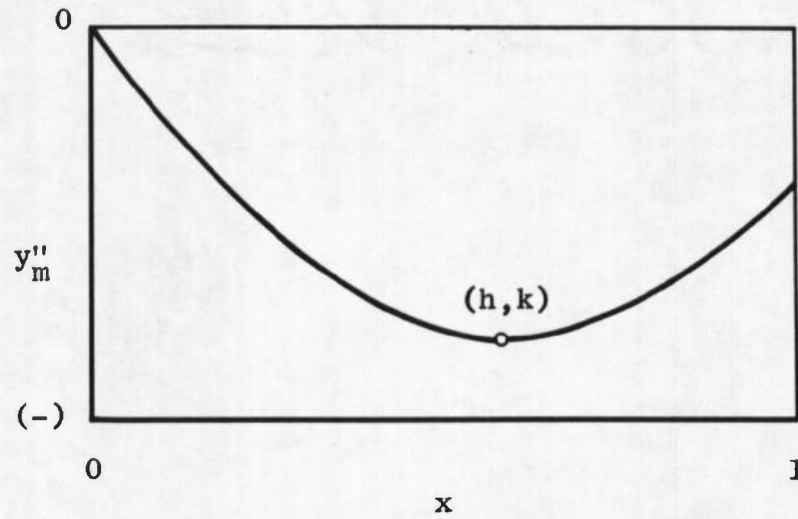


Fig. 1 Second Derivative of the Mean Chord Line

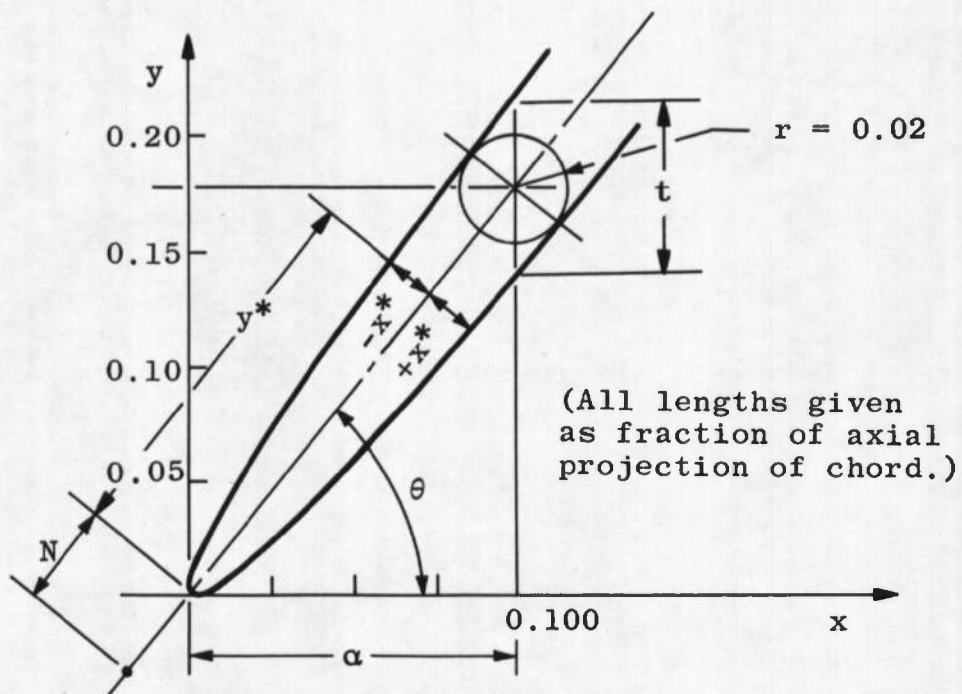
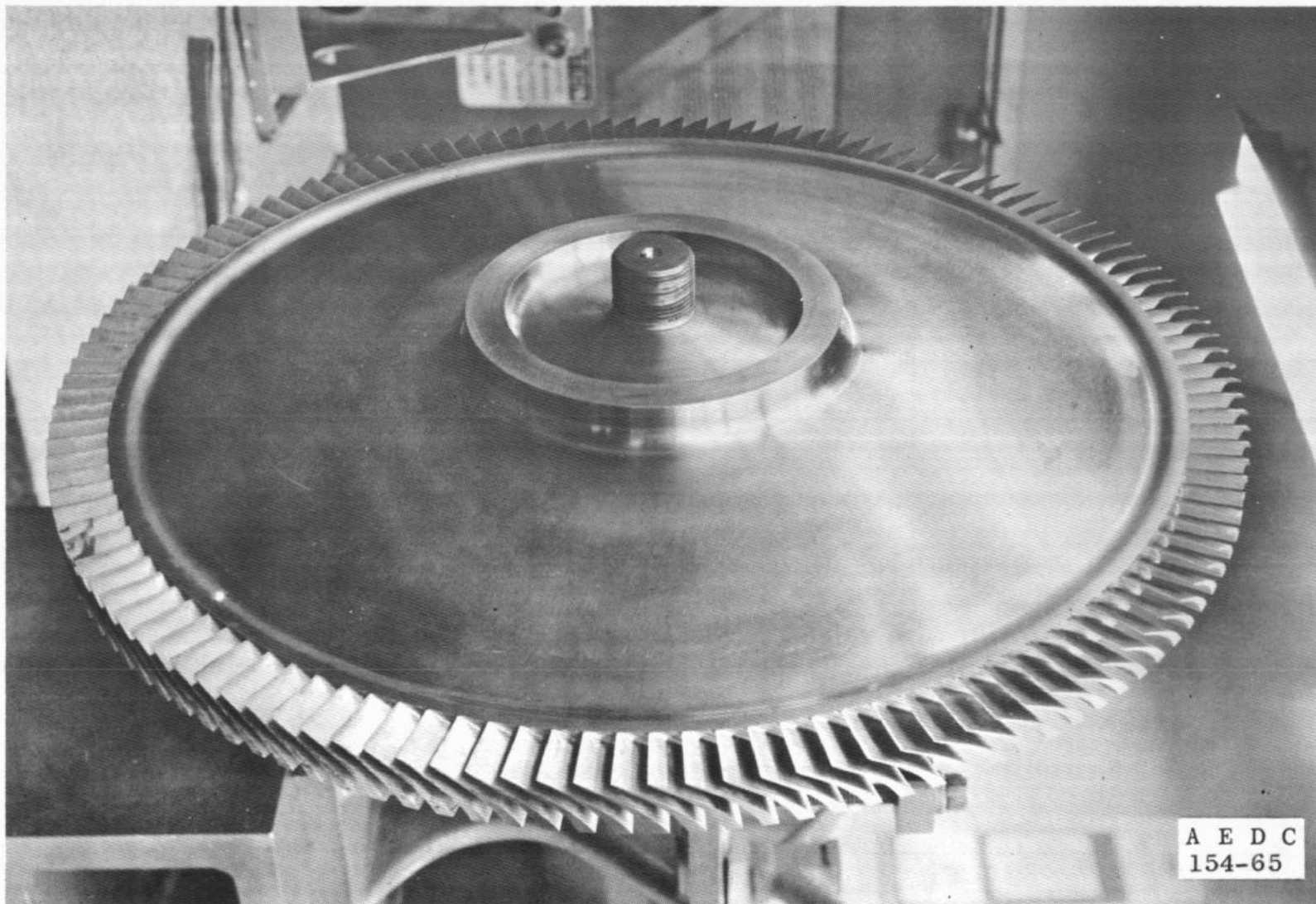
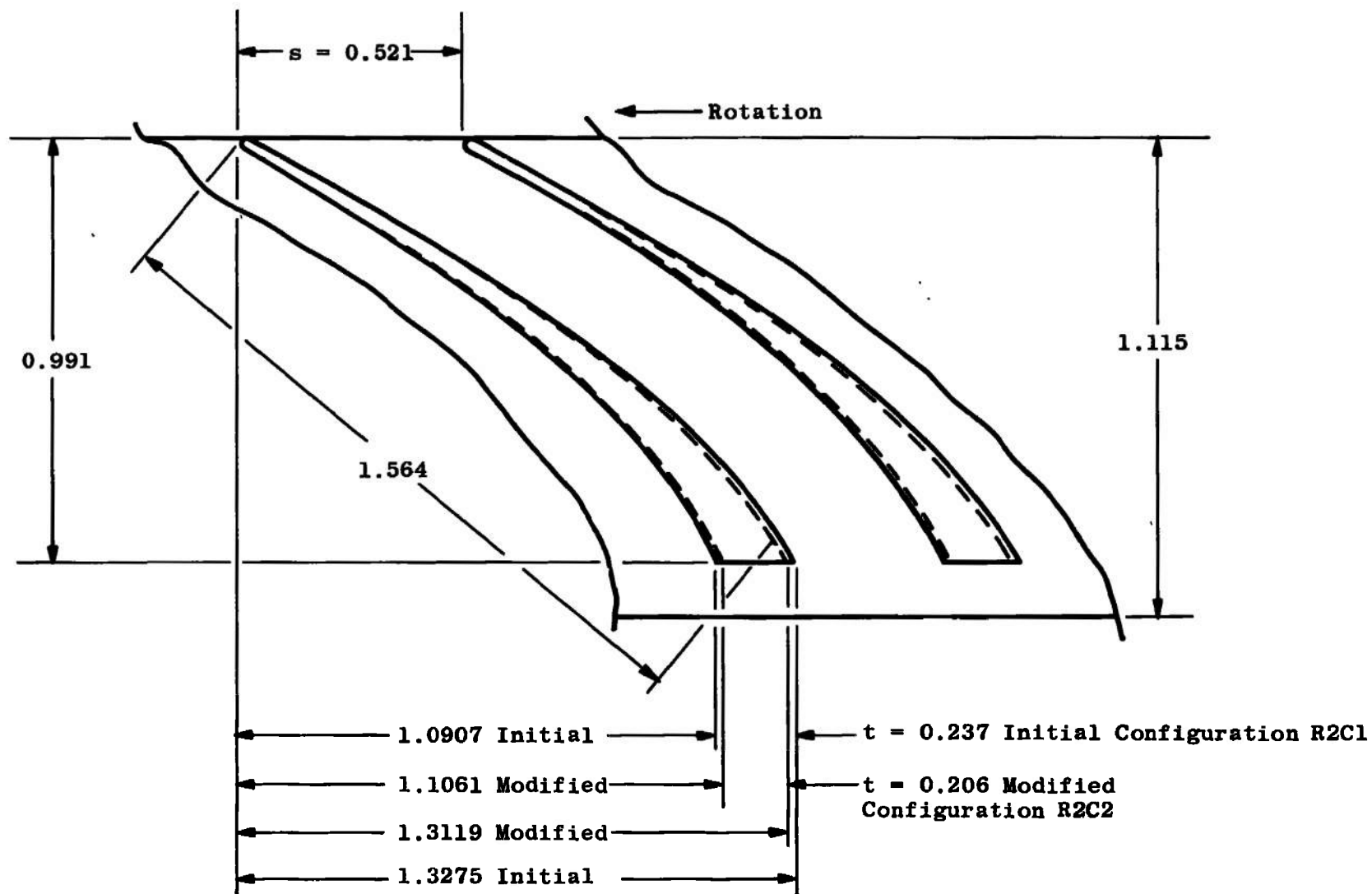


Fig. 2 Leading-Edge Profile



a. Overall View of the Rotor and Blading
Fig. 3 Compressor Rotor No. 2



b. Comparison of the Initial and Modified Blade Profiles of Configurations R2C1 and R2C2

Fig. 3 Concluded

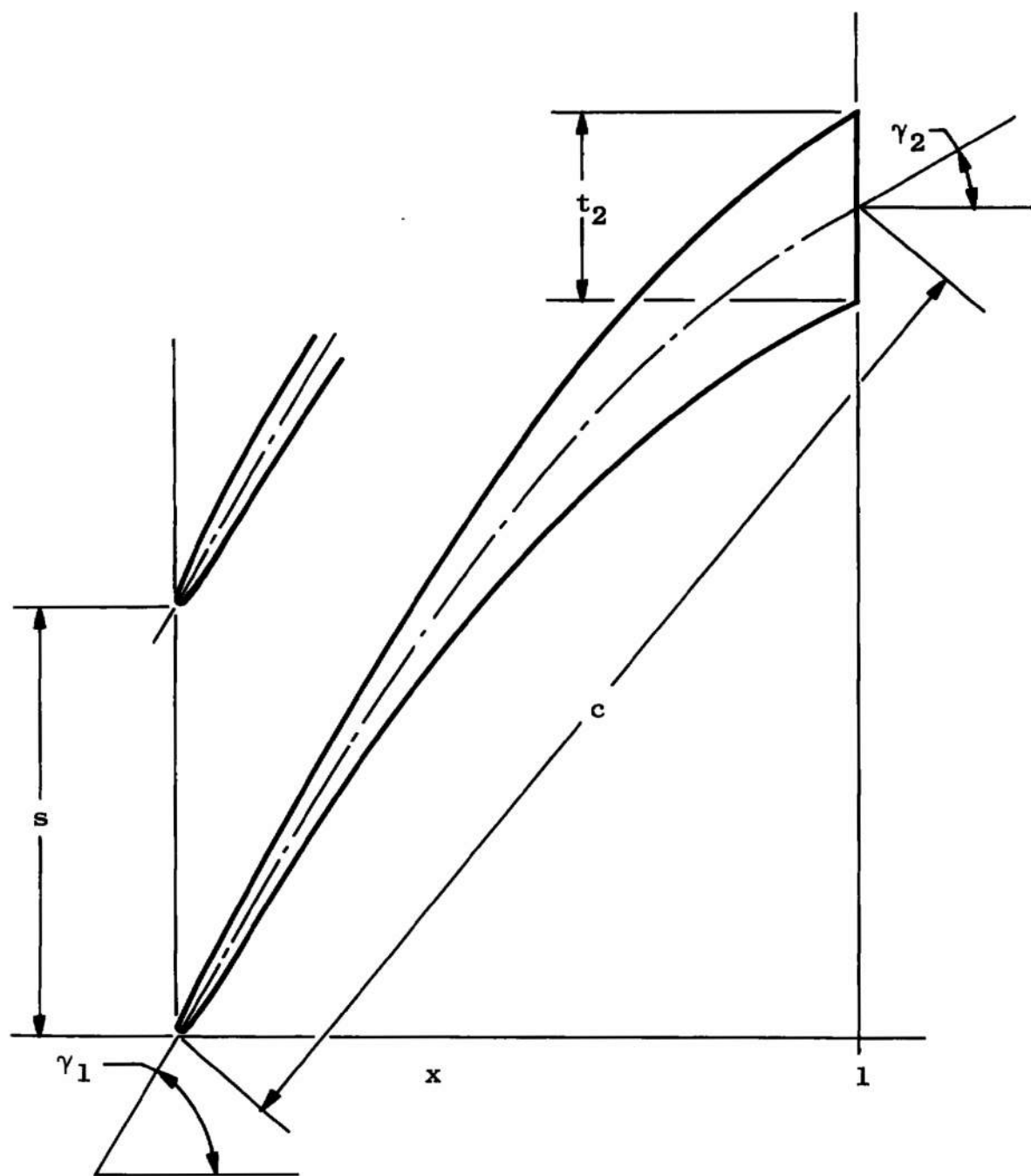


Fig. 4 Cascade Geometry

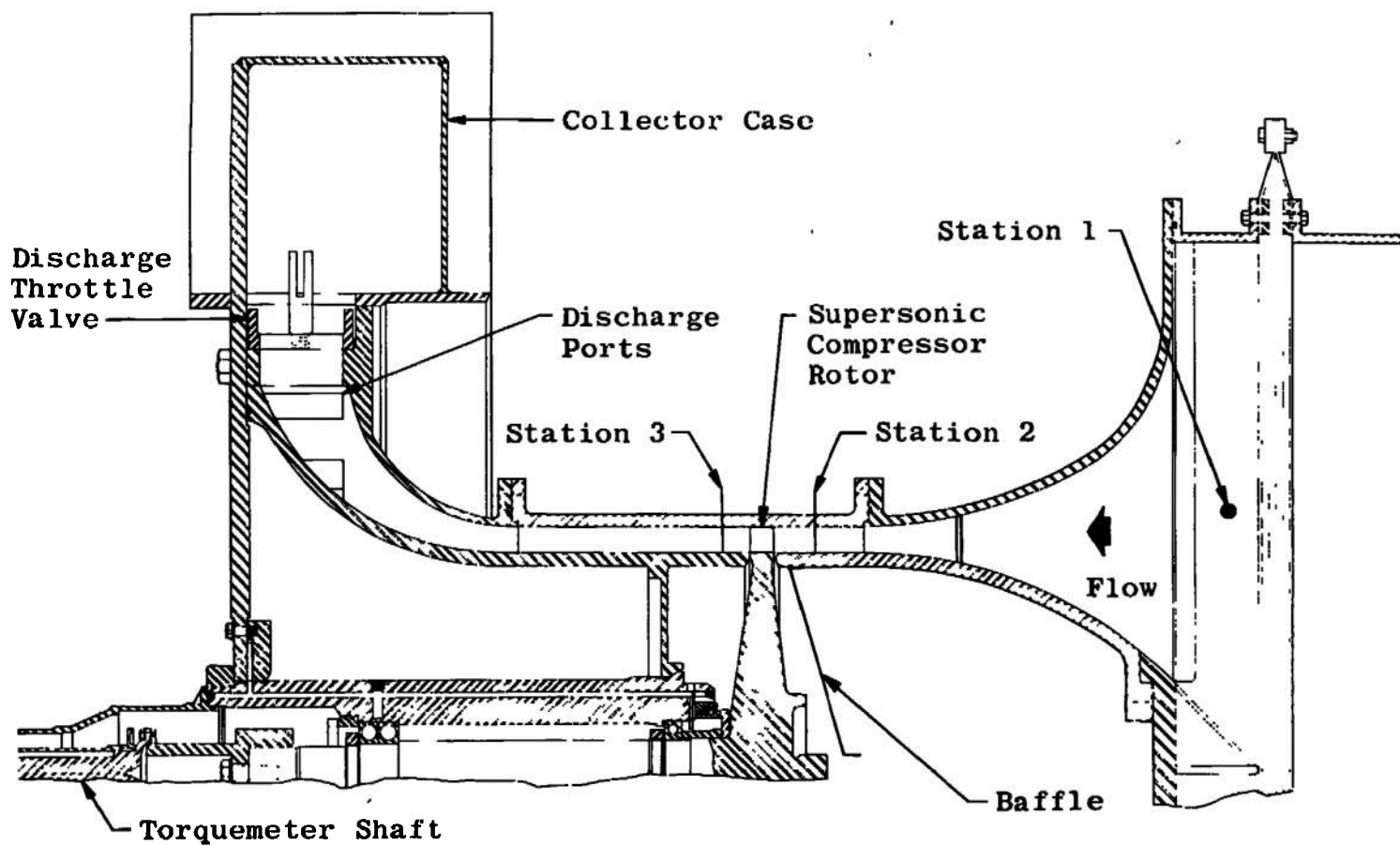


Fig. 5 Cross-Sectional View of Experimental Compressor

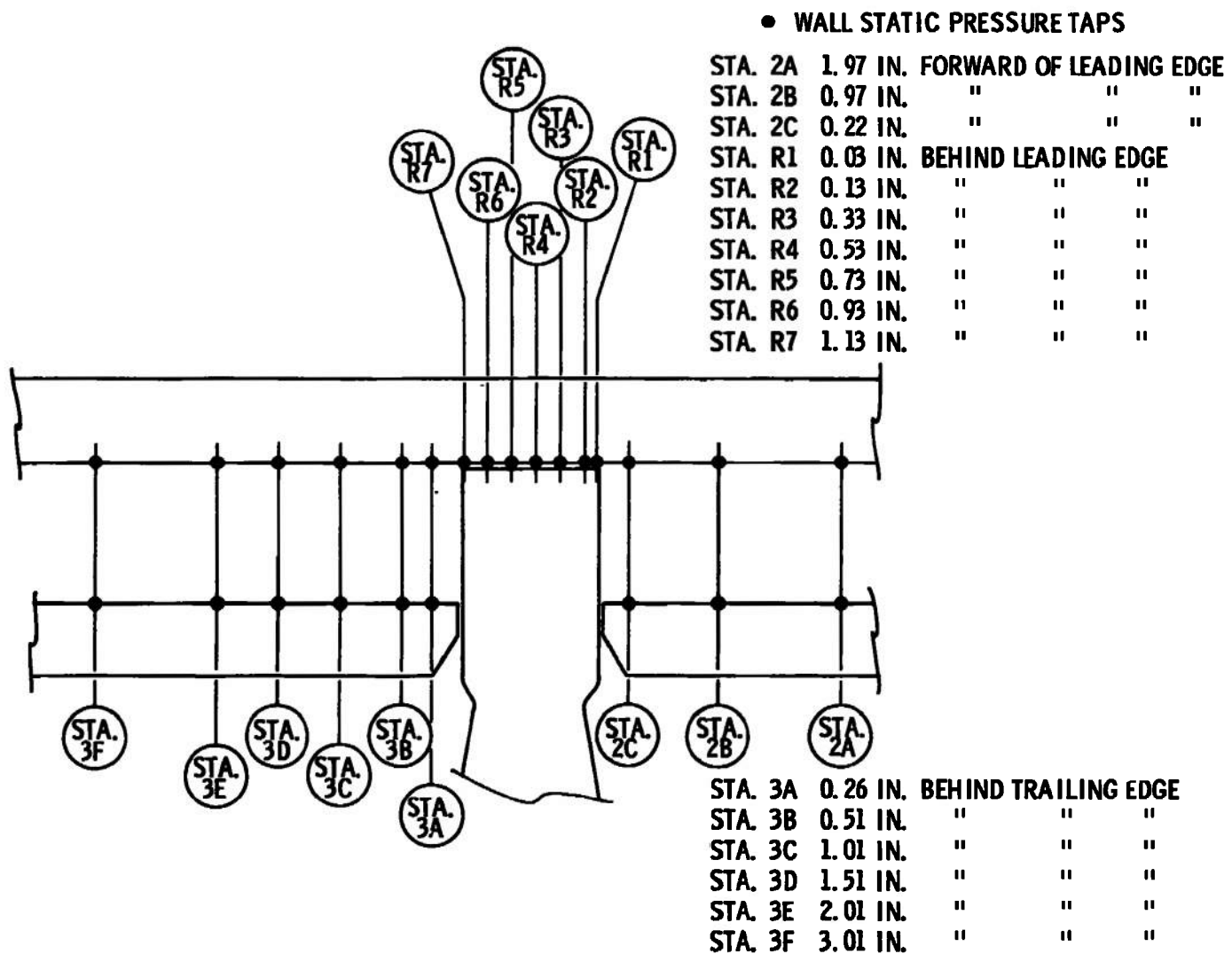


Fig. 6 Details of Instrumentation Stations

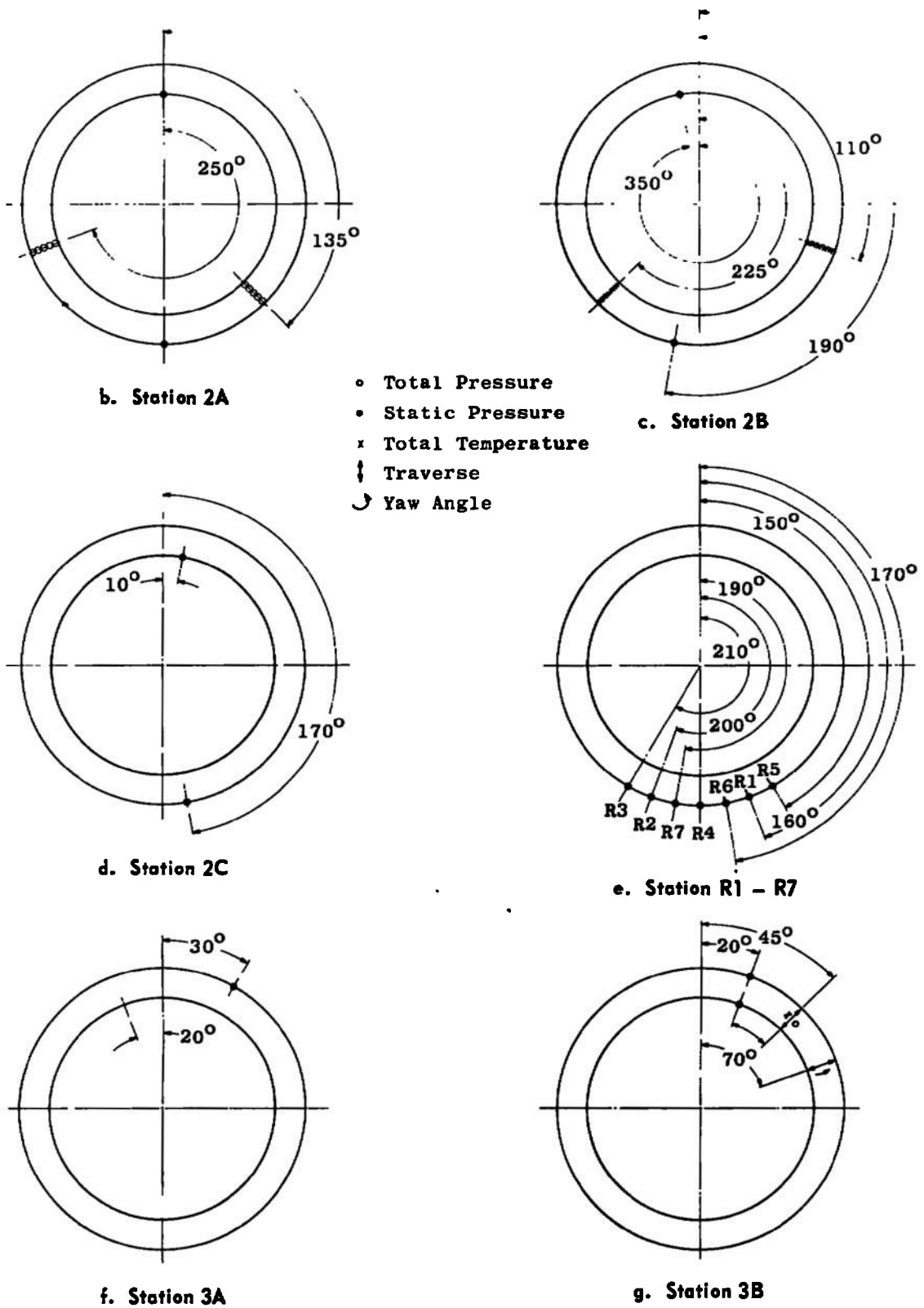
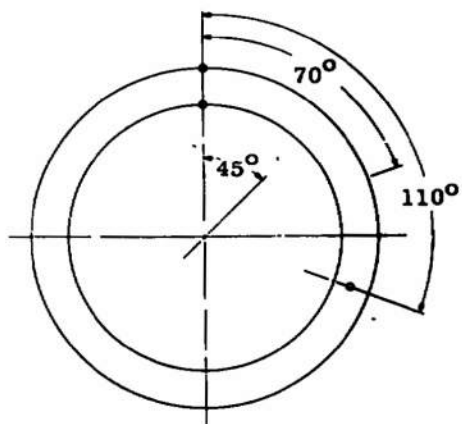
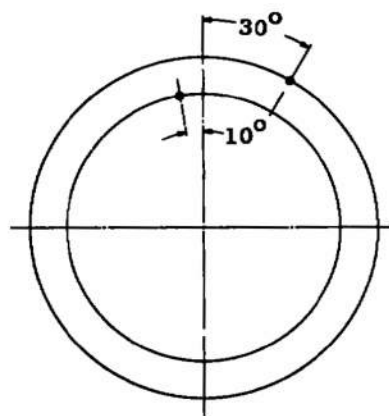


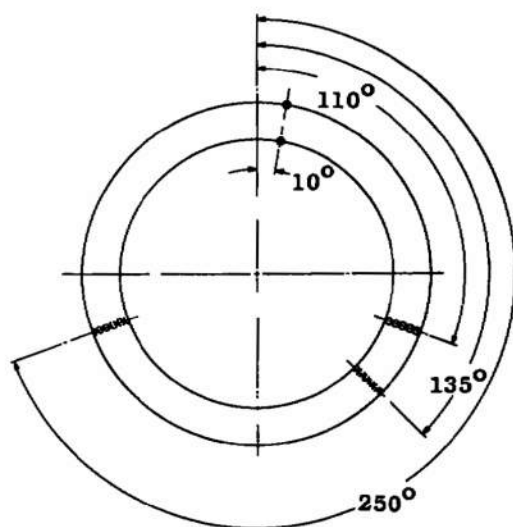
Fig. 6 Continued



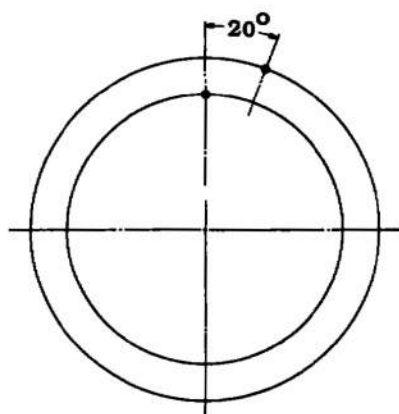
h. Station 3C



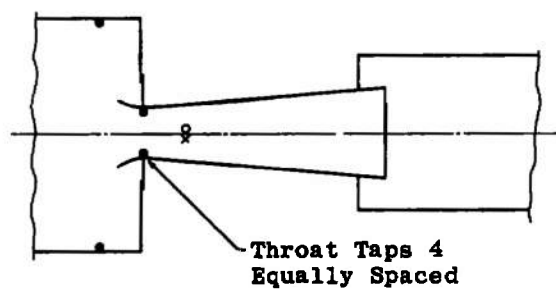
i. Station 3D



j. Station 3E



k. Station 3F



l. Venturi Instrumentation

Fig. 6 Concluded

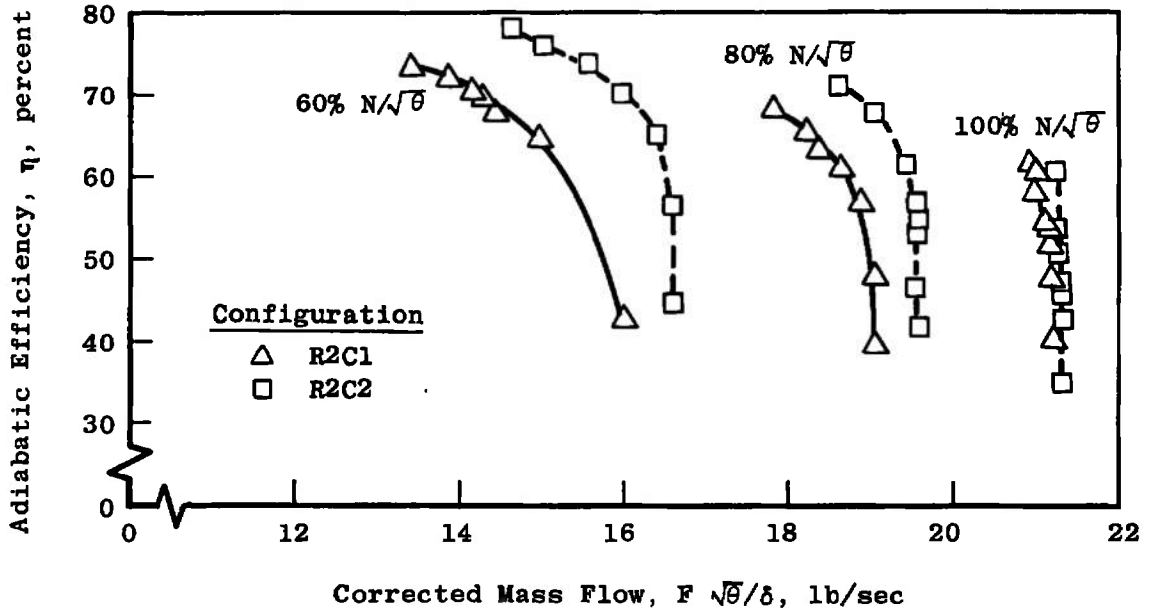


Fig. 7 Comparison of Rotor Efficiencies, R2C1 and R2C2

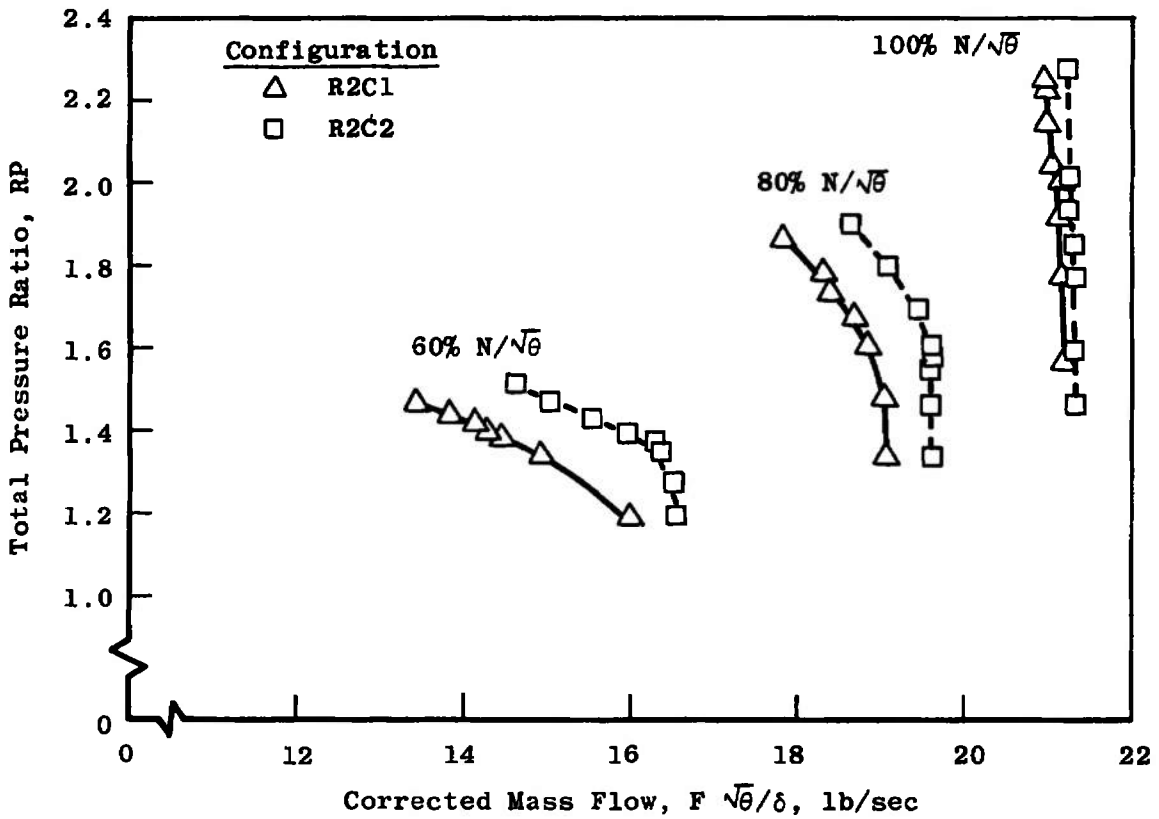


Fig. 8 Comparison of Rotor Total Pressure Ratio, R2C1 and R2C2

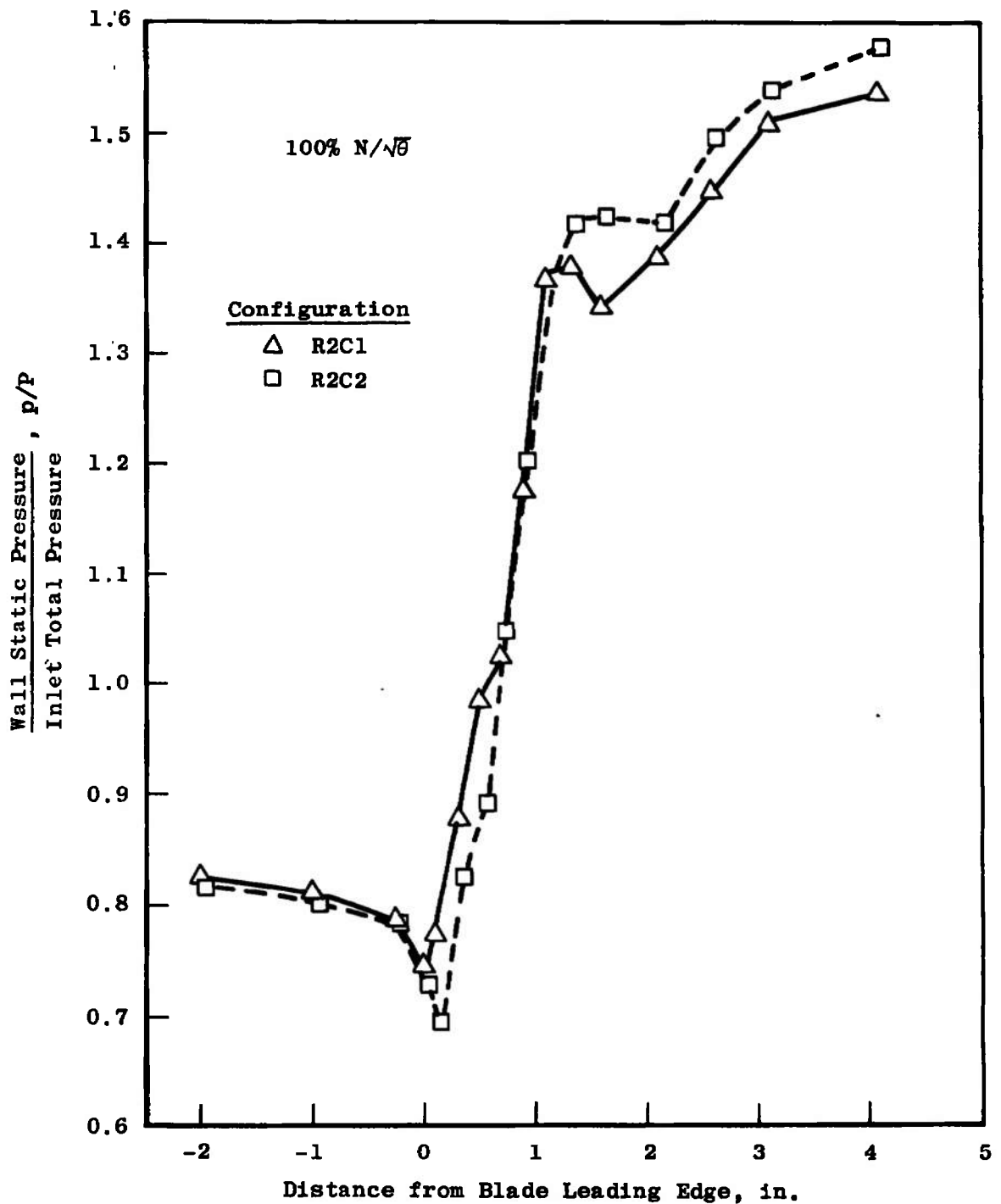


Fig. 9 Comparison of Static Pressure Axial Profiles, 100-percent Speed, R2C1 and R2C2

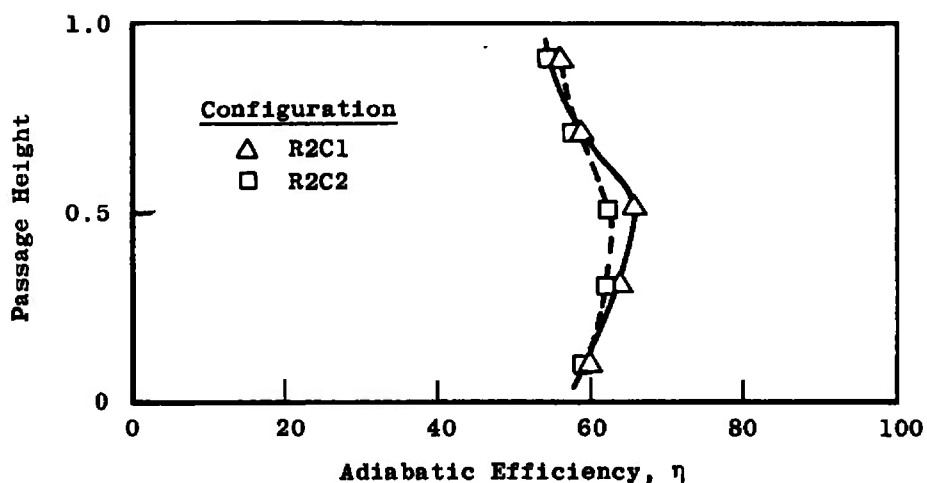


Fig. 10 Efficiency Distribution at Design Speed and Maximum Back Pressure, R2C1 and R2C2

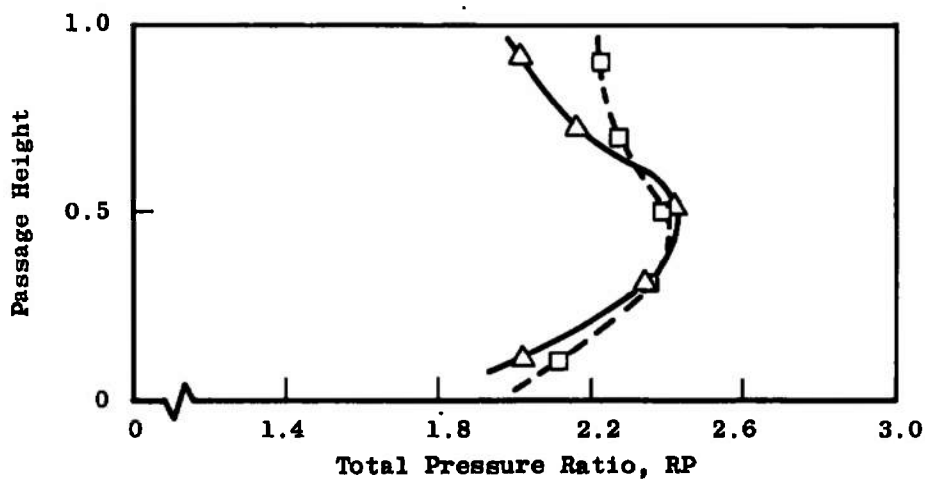


Fig. 11 Total Pressure Distribution at Design Speed and Maximum Back Pressure, R2C1 and R2C2

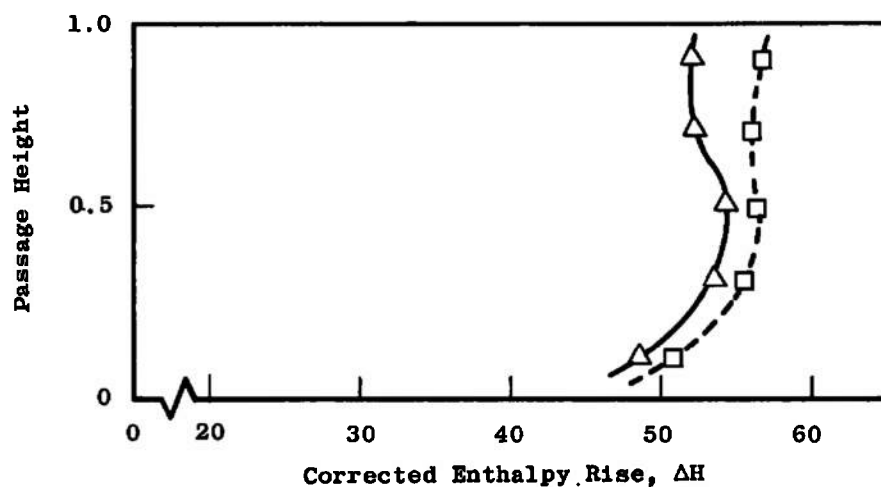


Fig. 12 Corrected Enthalpy Rise at Design Speed and Maximum Back Pressure, R2C1 and R2C2

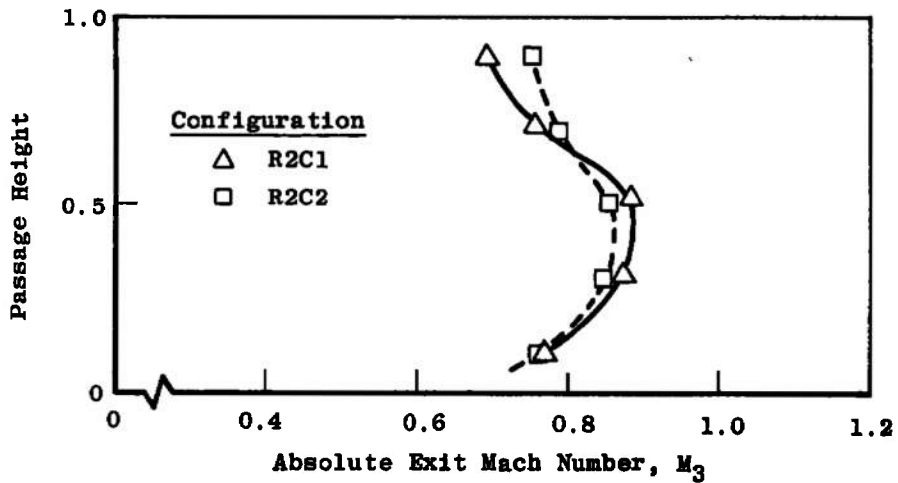


Fig. 13 Absolute Exit Mach Number Distribution at Design Speed and Maximum Back Pressure, R2C1 and R2C2

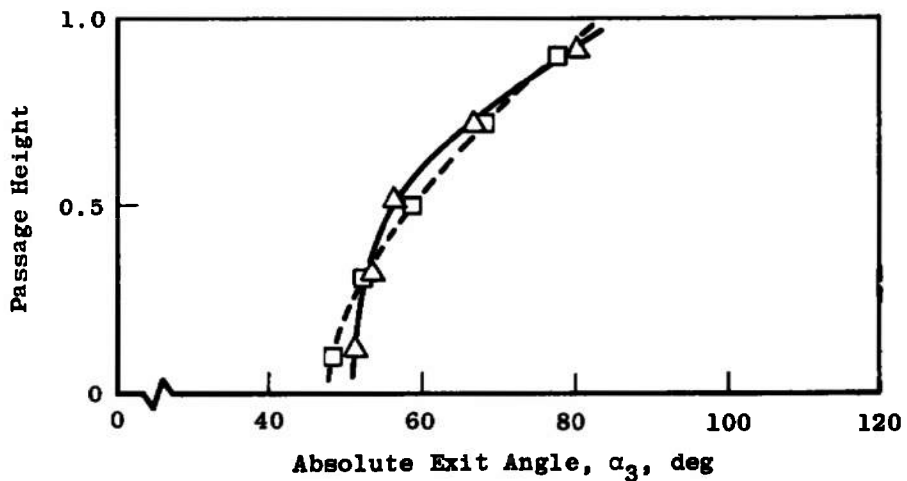


Fig. 14 Absolute Exit Angle Distribution at Design Speed and Maximum Back Pressure, R2C1 and R2C2

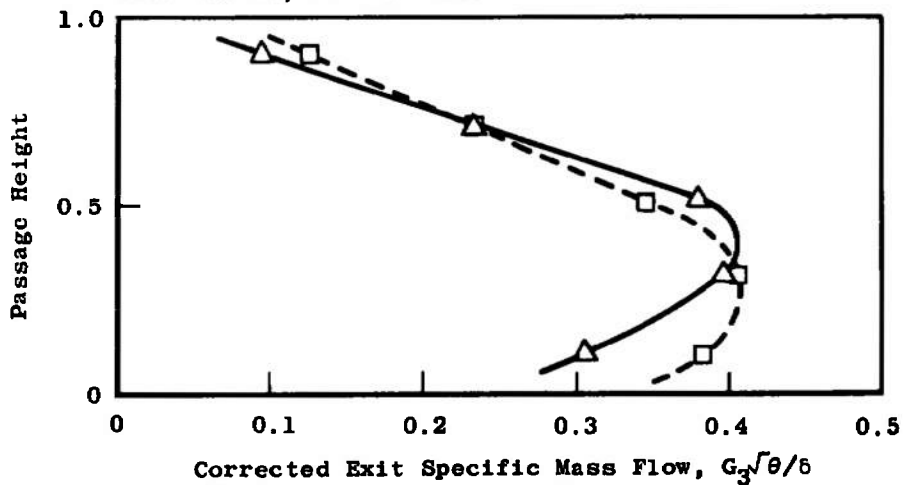


Fig. 15 Specific Mass Flow Distribution at Design Speed and Maximum Back Pressure, R2C1 and R2C2

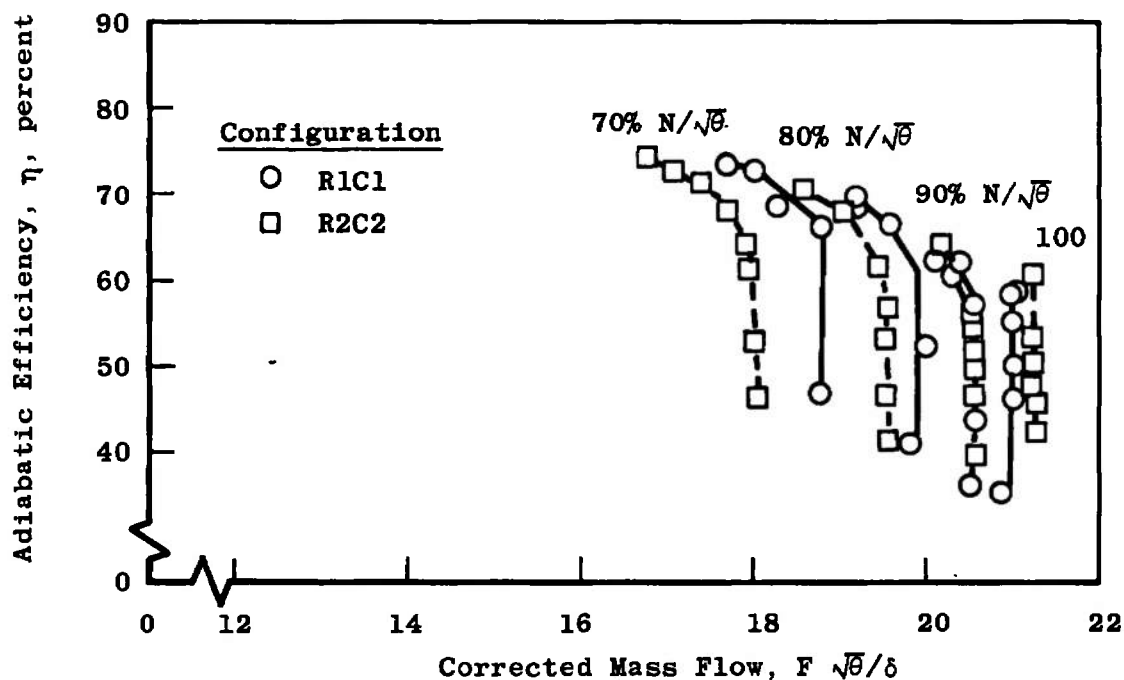


Fig. 16 Comparison of Rotor Efficiencies, R1C1 and R2C2

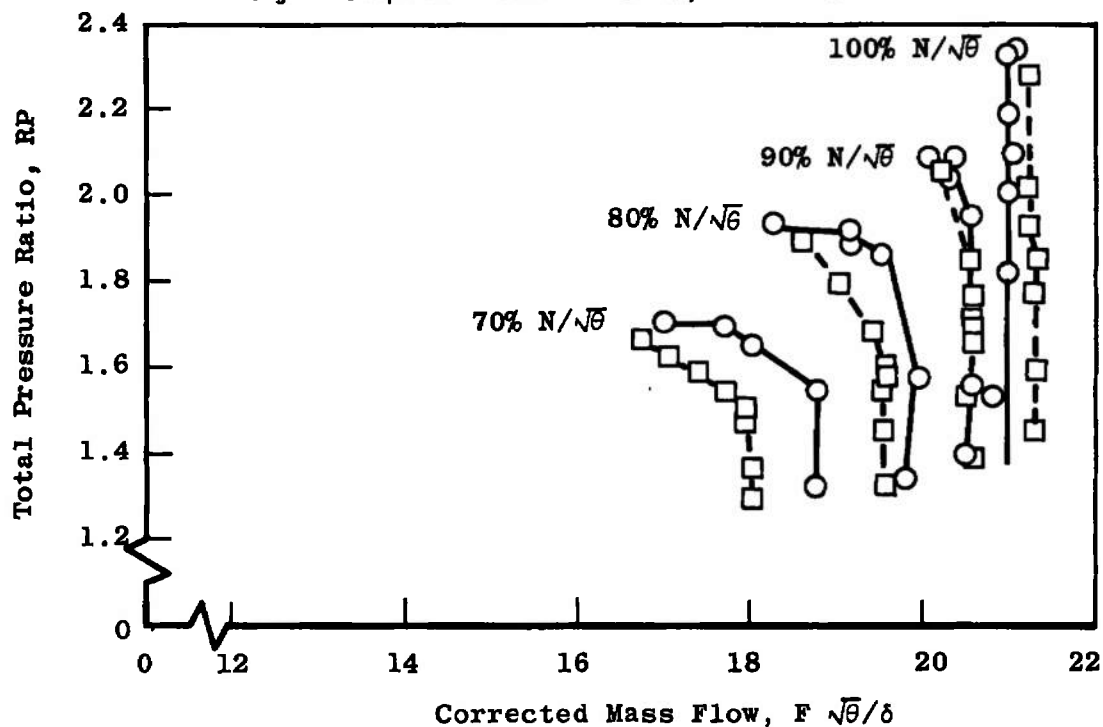


Fig. 17 Comparison of Rotor Total Pressure Ratio, R1C1 and R2C2

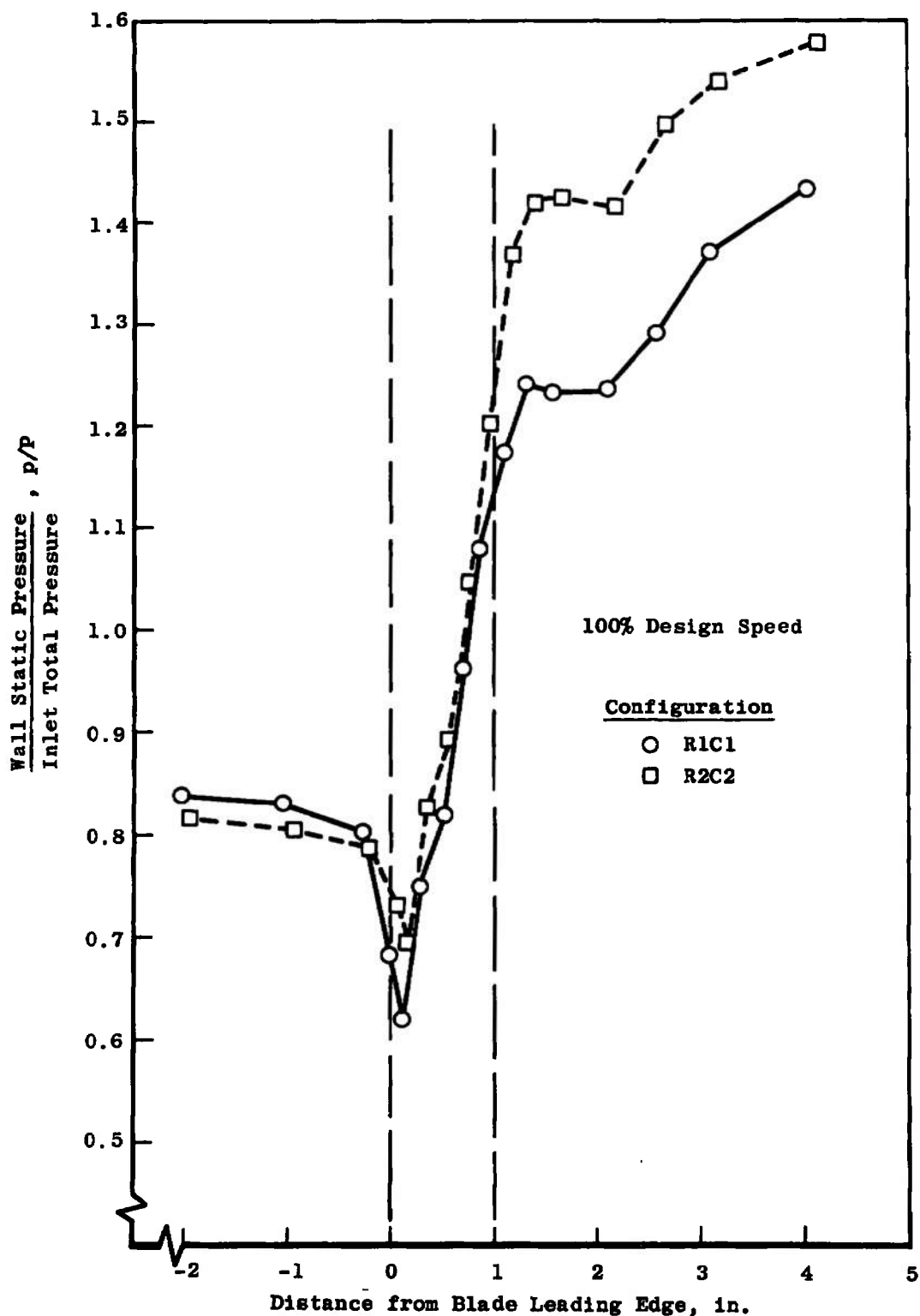


Fig. 18 Comparison of Static Pressure Axial Profiles, 100 Percent Speed, R1C1 and R2C2

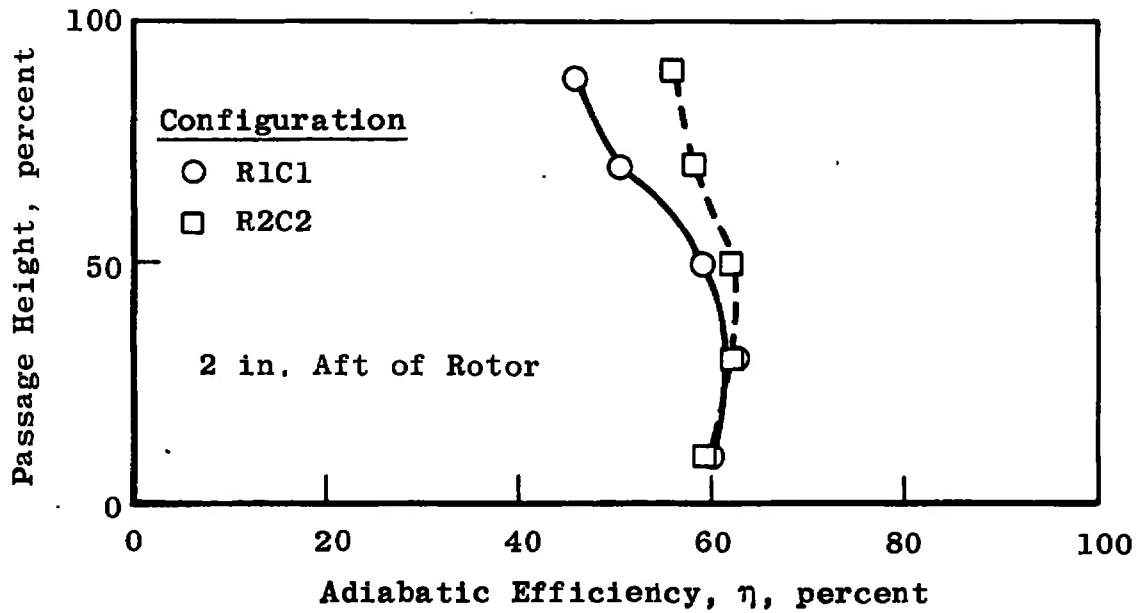


Fig. 19 Efficiency Distribution at Design Speed and Maximum Back Pressure, R1C1 and R2C2

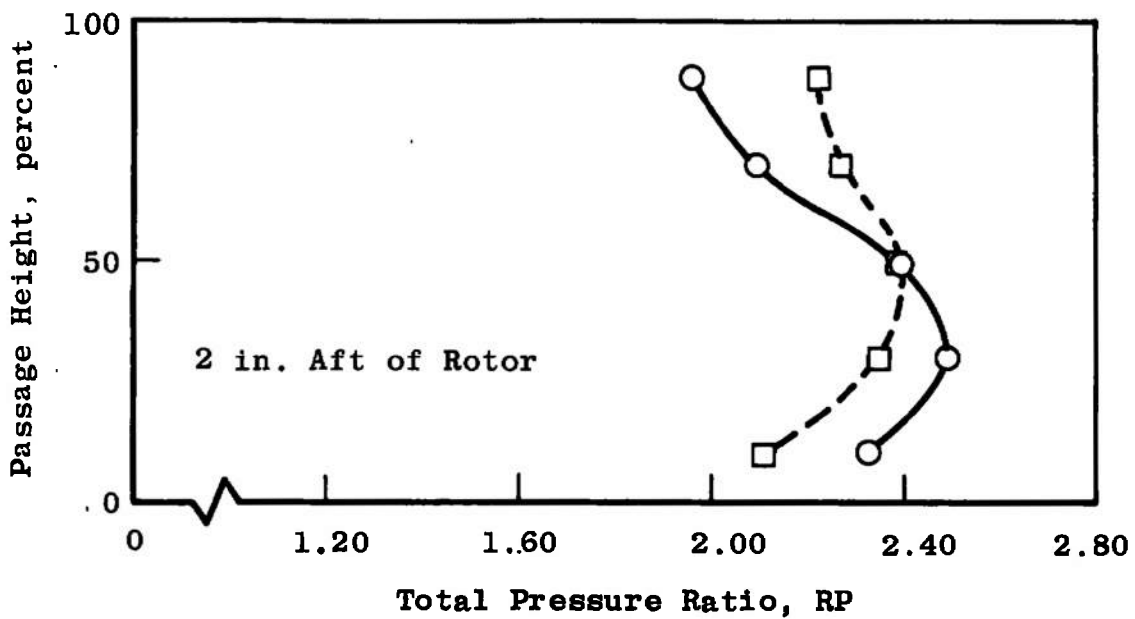


Fig. 20 Total Pressure Distribution at Design Speed and Maximum Back, Pressure, R1C1 and R2C2

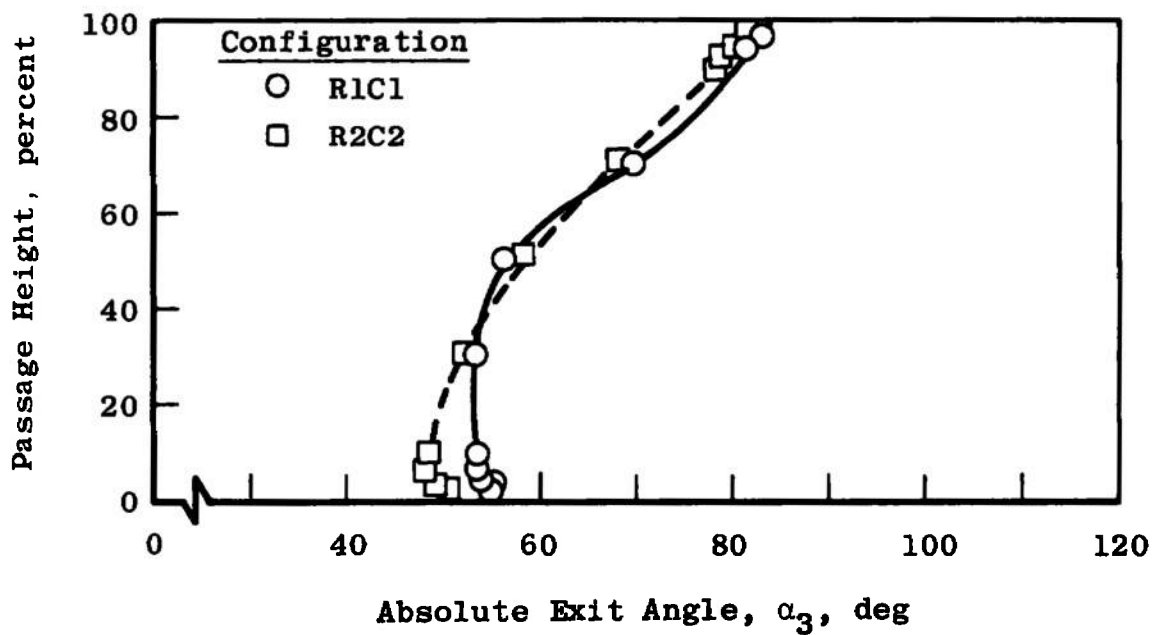


Fig. 21 Absolute Flow Angle at Design Speed and Maximum Back Pressure, R1C1 and R2C2

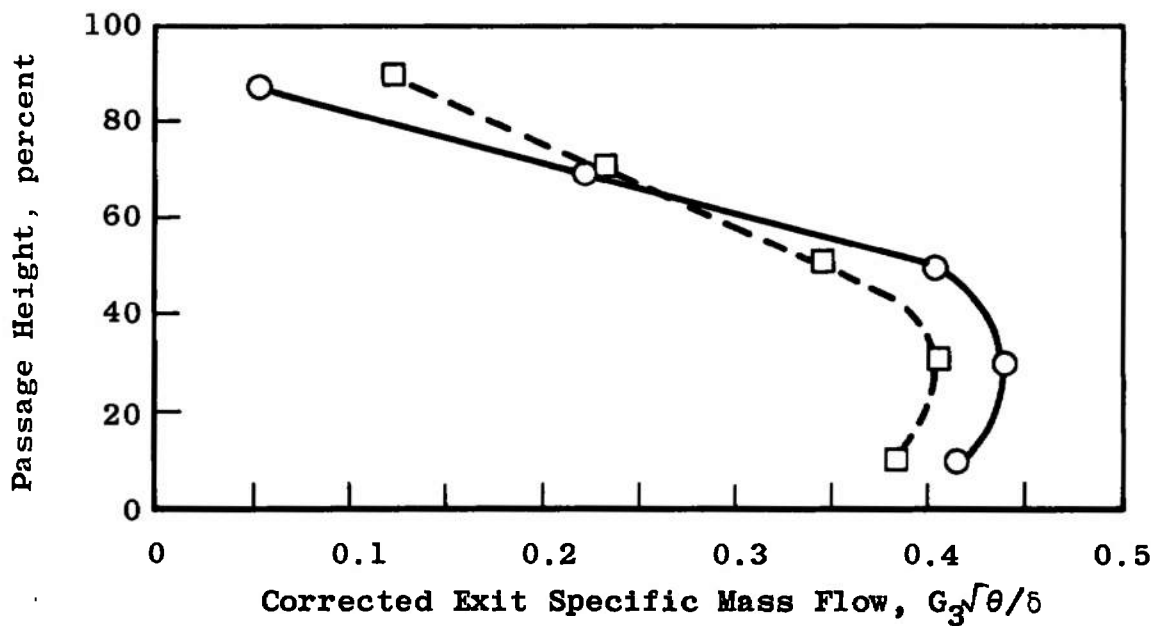


Fig. 22 Corrected Exit Specific Mass Flow at Design Speed and Maximum Back Pressure, R1C1 and R2C2

TABLE I
MIDRADIUS ROTOR BLADE COORDINATES FOR R2C1

C/S = 3.000, GAMMA1 = 60.000, GAMMA2 = 30.000
STT = 0. , HT = 0. , STH = 0. , HH = 0.
R = 0.0200, ALP = 0.100, BETA = 0.600, OMEGA = 0.100

XS	YS	XP	YP
-0.	0.	0.	-0.
0.0032879	0.0210037	0.0165301	0.0133203
0.0107017	0.0396081	0.0289342	0.0290294
0.0188415	0.0577810	0.0406125	0.0451492
0.0273658	0.0757152	0.0519062	0.0614765
0.0361378	0.0934853	0.0629522	0.0779271
0.0450855	0.1111279	0.0738225	0.0944542
0.0541652	0.1286637	0.0845608	0.1110278
0.0633482	0.1461047	0.0951958	0.1276263
0.0726142	0.1634579	0.1057478	0.1442334

X	YM	YS	YP
0.0990900	0.1707817	0.2099848	0.1315786
0.1486350	0.2546477	0.2955143	0.2137811
0.1981800	0.3367822	0.3802937	0.2932708
0.2477250	0.4167197	0.4637428	0.3696966
0.2972700	0.4940514	0.5453325	0.4427702
0.3468150	0.5684251	0.6245854	0.5122647
0.3963600	0.6395454	0.7010762	0.5780145
0.4459050	0.7071734	0.7744329	0.6399139
0.4954500	0.7711269	0.8443376	0.6979162
0.5449949	0.8312805	0.9105291	0.7520319
0.5945399	0.8875652	0.9728038	0.8023266
0.6440849	0.9399688	1.0310196	0.8489180
0.6936299	0.9885357	1.0850987	0.8919728
0.7431749	1.0333671	1.1350319	0.9317023
0.7927199	1.0746207	1.1808824	0.9683589
0.8422649	1.1125108	1.2227894	1.0022322
0.8918099	1.1473085	1.2609702	1.0336468
0.9413549	1.1793415	1.2957205	1.0629625
0.9908999	1.2089943	1.3274110	1.0905775

T2 = 0.5804558

C = 1.5681859

S = 0.5210819

TABLE II
MIDRADIUS ROTOR BLADE COORINATES FOR R2C2

C/S = 3.000, GAMMA1 = 60.000, GAMMA2 = 30.000

STT = 0, HT = 0, STH = 0, HH = 0.

R = 0.0200, ALP = 0.100, BETA = 0.600, OMEGA = 0.220

XS	YS	XP	YP
-0.	0.	0.	-0.
0.0032879	0.0210037	0.0165301	0.0133203
0.0107017	0.0396081	0.0289342	0.0290294
0.0188415	0.0577810	0.0406125	0.0451492
0.0273658	0.0757152	0.0519062	0.0614765
0.0361378	0.0934853	0.0629522	0.0779271
0.0450855	0.1111279	0.0738225	0.0944542
0.0541652	0.1286637	0.0845608	0.1110278
0.0633482	0.1461047	0.0951958	0.1276263
0.0726142	0.1634579	0.1057478	0.1442334

X	YM	YS	YP
0.0990900	0.1707817	0.2099848	0.1315786
0.1486350	0.2546477	0.2940580	0.2152375
0.1981800	0.3367822	0.3774319	0.2961326
0.2477250	0.4167197	0.4595426	0.3738968
0.2972700	0.4940514	0.5398738	0.4482289
0.3468150	0.5684251	0.6179572	0.5188930
0.3963600	0.6395454	0.6933730	0.5857177
0.4459050	0.7071734	0.7657511	0.6485956
0.4954500	0.7711269	0.8347723	0.7074815
0.5449949	0.8312805	0.9001701	0.7623909
0.5945399	0.8875652	0.9617327	0.8133977
0.6440849	0.9399688	1.0193068	0.8606308
0.6936299	0.9885357	1.0728011	0.9042704
0.7431749	1.0333671	1.1221909	0.9445433
0.7927199	1.0746207	1.1675230	0.9817183
0.8422649	1.1125108	1.2089199	1.0161016
0.8918099	1.1473085	1.2465830	1.0480340
0.9413549	1.1793415	1.2807931	1.0778899
0.9908999	1.2089943	1.3119077	1.1060808

T2 = 0.5804558

C = 1.5631859

S = 0.5210619

APPENDIX III MEASUREMENT UNCERTAINTY

Physical measurements involve two basic classes of error - precision or repeatability error and accuracy error. Precision error is present when successive measurements of an unchanged quantity yield different numerical results. Accuracy error is present when the numerical average of successive readings deviates from the known correct reading and continues to do so no matter how many successive readings are taken.

Accuracy error is eliminated by calibration. The total pressure probes have been calibrated aerodynamically. Total temperature probes have been calibrated in an oil bath (see references).

Without a great many replications of readings with the entire measurement system, precision error can only be estimated from manufacturers' specifications for each component of the system. Tables III-I and III-II show the estimated precision for the instrumentation used for these tests. In these tables the system sensor implies the transducer in the case of pressure measurements and the thermocouple junction for the temperature measurements. Transmission error for temperature measurements depends on the wire used. Reference errors may involve the accuracy in reading atmospheric pressure or some base reference. Read-out error includes both interpretation and digitizing error. The total precision is the arithmetic sum of these values. If calibration has been used to eliminate accuracy error, these figures represent the total uncertainty of a single measurement.

The final column of Tables III-I and III-II presents the number of times a single point is replicated. Traverse measurements are manually read while rake data are electronically recorded. During one traverse there is time to make three complete scans of rake data. Since error in an average is inversely proportional to the square of the number of readings making up the average,¹ it is felt that the rake measurements probably represent the more accurate values.

The precision index W_R of a general function R where

$$R = f(x_1, x_2, \dots, x_n)$$

¹Hilbert, Shenck, Jr. Theories of Engineering Experimentation. McGraw-Hill Book Company, New York, N. Y., 1961.

may be calculated by

$$W_R = \left[\sum_{i=1}^n \left(\frac{\partial R}{\partial x_i} \right)^2 w_i^2 \right]^{1/2}$$

where W_i is the precision of the independent variables. Using this relation and the estimated precision of Tables III-I and III-II and assuming constant specific heat at constant pressure, the estimated precision in total pressure ratio, RP, adiabatic efficiency, η , inlet absolute Mach number, M_2 , and outlet absolute Mach number, M_3 , is calculated at the extremes of operating conditions. Inlet stagnation conditions are assumed standard.

The following table summarizes the results of the computation where the precisions indicated represent approximately twice the standard deviation.

CONFIGURATION 1

	W_{RP}	W_N	W_{M_2}	W_{M_3}
1.0N Max	± 0.021	± 0.017	± 0.004	± 0.001
0.5N Min	± 0.013	± 0.088	± 0.005	± 0.004

CONFIGURATION 2

	W_{RP}	W_N	W_{M_2}	W_{M_2}
1.0N Max	± 0.014	± 0.015	± 0.002	± 0.001
0.5N Min	± 0.011	± 0.072	± 0.002	± 0.004

The apparent large uncertainty in efficiency at low-speed operation is not born out in repeated measurements near this condition. Precision in efficiency based on seven data points at 0.6N minimum pressure ratio is computed to be approximately ± 0.020 .

Mass flow is measured by a venturi flowmeter with manometer board pressure measurements photographically recorded and temperature measurements recorded electronically. The precision of the mass flow measurements at 1.0N maximum pressure ratio is computed to be approximately $\pm 0.415 \text{ lb}_m/\text{sec}$. This value includes allowance for error in readings of atmospheric pressure and fluid column heights; fluid density change caused by variation in ambient temperature and manometer board temperature gradients; sensor, transmission, reference and read-out errors in temperature; round-off errors in millivolt to Fahrenheit degree conversion; venturi throat area measurement precision; and the flow coefficient.

Rpm is measured by a frequency counter for the output of an electromagnetic pickup. The accuracy is ± 1 count digitizing error, ± 0.04 percent of the reading caused by scale conversion, ± 10 counts error in reading during operation. At maximum rpm this amounts to ± 0.1 percent error.

**TABLE III-I
CONFIGURATIONS R2C1 AND R2C2**

<u>Parameter</u>	<u>Sensor Precision</u>	<u>Transmission Precision</u>	<u>Reference Precision</u>	<u>Read-Out Precision</u>	<u>Total Precision</u>	<u>Repetition</u>
<u>Total Pressure</u>						
Inlet Rake	±0.050 psi			±0.015 psi	±0.065 psi	6
Outlet Rake	±0.125 psi			±0.015 psi	±0.140 psi	3
Outlet Traverse	±0.125 psi			±0.125 psi	±0.250 psi	1
<u>Static Pressure</u>						
Inlet Wall 2A, 2B, 2C	±0.050 psi			±0.015 psi	±0.065 psi	3
Wheel Wall TR1, 2, 3	±0.050 psi			±0.015 psi	±0.065 psi	3
TR4	±0.075 psi			±0.015 psi	±0.090 psi	3
TR5, 6, 7	±0.500 psi		±0.005 psi	±0.015 psi	±0.520 psi	3
Outlet Wall 3A, 3B, 3E, 3F	±0.125 psi			±0.015 psi	±0.140 psi	3
3C, 3D	±0.500 psi		±0.005 psi	±0.015 psi	±0.520 psi	3
<u>Total Temperature</u>						
Inlet Rake	±1°R	±2.0°R	±0.200°R	±0.006 MV(0.324°R)	±3.524°R	6
Outlet Rake	±1°R	±2.0°R	±0.200°R	±0.006 MV(0.324°R)	±3.524°R	6
Outlet Traverse	±1°R	±2.0°R	±0.875°R	±1.0°R	±4.875°R	1
<u>Absolute Flow Angle</u>	±0.25 deg		±0.50 deg	±0.50 deg	±1.25 deg	1

TABLE III-II
CONFIGURATION R2C1

<u>Parameter</u>	<u>Sensor Precision</u>	<u>Transmission Precision</u>	<u>Reference Precision</u>	<u>Read-Out Precision</u>	<u>Total Precision</u>	<u>Repetition</u>
<u>Total Pressure</u>						
Inlet Rake	±0.100 psi		±0.005 psi	±0.015 psi	±0.120 psi	6
Outlet Rake	±0.125 psi			±0.015 psi	±0.140 psi	3
Outlet Traverse	±0.125 psi			±0.125 psi	±0.250 psi	
<u>Static Pressure</u>						
Inlet Wall 2A, 2B, 2C	±0.100 psi		±0.005 psi	±0.015 psi	±0.120 psi	3
Wheel Wall TR1, 2, 3, 4	±0.100 psi		±0.005 psi	±0.015 psi	±0.120 psi	3
TR5, 6, 7	±0.500 psi		±0.005 psi	±0.015 psi	±0.520 psi	3
Outlet Wall 3A, 3B, 3E, 3F	±0.125 psi			±0.015 psi	±0.140 psi	3
3C, 3D	±0.500 psi		±0.005 psi	±0.015 psi	±0.520 psi	3
<u>Total Temperature</u>						
Inlet Rake	±1°R	±2.0°R	±0.200°R	±0.006MV(0.324°R)	±3.524°R	6
Outlet Rake	±1°R	±2.0°R	±0.200°R	±0.006MV(0.324°R)	±3.524°R	6
Outlet Traverse	±1°R	±2.0°R	±0.875°R	±1.0°R	±4.875°R	1
<u>Absolute Flow Angle</u>	±0.25 deg		±0.50 deg	±0.50 deg	±1.25 deg	1

APPENDIX IV METHODS OF CALCULATION

General methods and equations employed to compute the parameters presented are given herein. Test data were processed to the final parameters with an IBM 360/50 digital computer.

TEMPERATURE

Discharge total temperatures were corrected by applying a recovery factor of 0.96 to the indicated temperature measurements in the calculation

$$T_s = \frac{T_i(\gamma M^2 - M^2 + 2)}{RF(\gamma M^2 - M^2) + 2}$$

Static temperatures were calculated from the measured stagnation temperatures and pressures by using perfect gas, isentropic relation

$$t = T \left(\frac{p}{P} \right)^{\frac{\gamma - 1}{\gamma}}$$

The static pressure values across the passage were assumed as a linear variation from the measured static pressures at the walls.

SPECIFIC HEAT

The specific heat at constant pressure was computed from the empirical equation

$$C_p = 0.2318 + 0.104 \times 10^{-4} T + 0.7166 \times 10^{-8} T^2$$

The ratio of specific heats was assumed to be 1.4 at the venturi and inlet stations. At all other stations the ratio of specific heats was calculated from the expression

$$\gamma = \frac{C_p}{C_p - \frac{R}{J}}$$

When applicable, arithmetic averages of the specific heat ratios were used.

AIRFLOW

Airflow was calculated at the venturi from the following equation using a flow coefficient (C_f) of 0.99:

$$F = C_f A P \left[\frac{2\gamma g}{RT(\gamma - 1)} \left(\left[\frac{P}{P} \right]^{\frac{2}{\gamma}} - \left[\frac{P}{P} \right]^{\frac{\gamma+1}{\gamma}} \right) \right]^{\frac{1}{2}}$$

ABSOLUTE MACH NUMBER

Mach number was obtained from the compressible flow equation

$$M = \left(\frac{2}{\gamma - 1} \right)^{\frac{1}{2}} \left[\left(\frac{P}{P} \right)^{\frac{\gamma - 1}{\gamma}} - 1 \right]^{\frac{1}{2}}$$

ADIABATIC EFFICIENCY

The adiabatic efficiency was computed from the following expressions:

$$\eta = \frac{\Delta H_{ideal}}{\Delta H_{actual}}$$

where

$$\Delta H = \int_{T_2}^{T_3} C_p dT$$

$$Ideal T_3 = T_2 \left(\frac{P_3}{P_2} \right)^{\frac{\gamma - 1}{\gamma}}$$

$$Actual T_3 = T_3 \text{ measured}$$

VELOCITY

Velocity was determined from the expression

$$C = \left(\frac{2\gamma R g t}{\gamma - 1} \right)^{\frac{1}{2}} \left[1 - \left(\frac{P}{P} \right)^{\frac{\gamma - 1}{\gamma}} \right]^{\frac{1}{2}}$$

RELATIVE FLOW ANGLE

Relative flow angle to the blade was obtained by

$$\beta = \arctan \frac{U - C \sin \alpha}{C \cos \alpha}$$

where

$$U = \frac{2\pi}{60} r N$$

RELATIVE MACH NUMBER

Relative Mach number to the blade was determined by

$$M_w = \frac{W}{C}$$

where

$$W = \frac{U - C \sin \alpha}{\sin \beta}$$

MASS-WEIGHTING FACTOR

Specific mass flow is used as a weighting factor in the summation of various parameters computed from data measured in the five equal areas across the annulus passage and is calculated by

$$G = pM \left(\frac{g\gamma}{RT} \right)^{\frac{1}{2}} \cos \alpha$$

APPENDIX V

DATA SUMMARY FOR CONFIGURATIONS R2C1 AND R2C2

ILLUSTRATIONS

Fig. V-1 Configuration R2C1

- a. Compressor Performance Characteristics Based on Equivalent Weight Flow
- b. Compressor Performance Characteristics Based on Weight Flow Ratio
- c. Inlet Parameters, $100\%N/\sqrt{\theta}$
- d. Exit Parameters, $100\%N/\sqrt{\theta}$
- e. Adiabatic Efficiency and Pressure Ratio,
 $100\%N/\sqrt{\theta}$
- f. Exit Specific Mass Flow and Enthalpy Rise,
 $100\%N/\sqrt{\theta}$

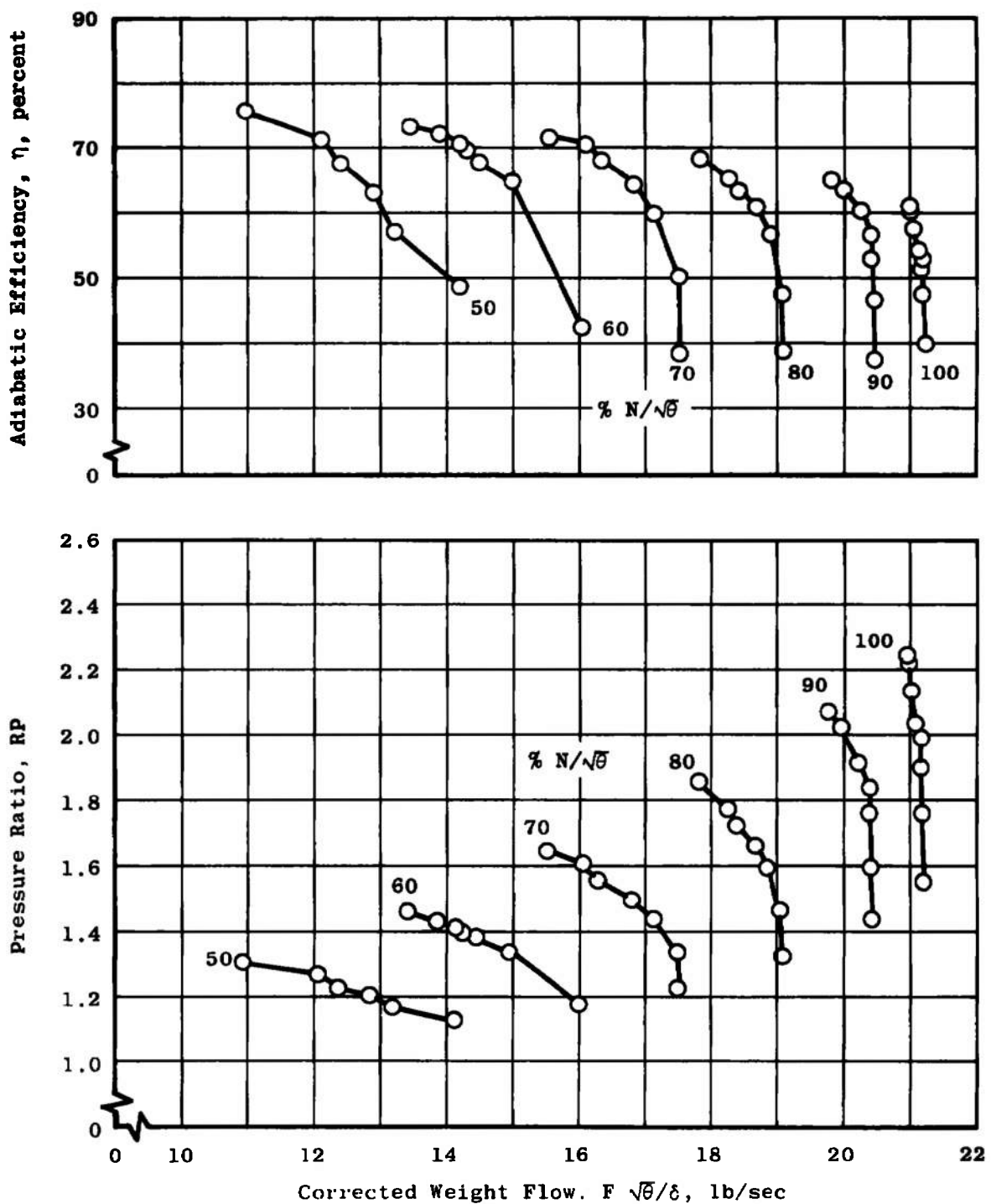
Fig. V-2 Configuration R2C2

- a. Compressor Performance Characteristics Based on Equivalent Weight Flow
- b. Compressor Performance Characteristics Based on Weight Flow Ratio
- c. Inlet Parameters, $100\%N/\sqrt{\theta}$
- d. Exit Parameters, $100\%N/\sqrt{\theta}$
- e. Adiabatic Efficiency and Pressure Ratio,
 $100\%N/\sqrt{\theta}$
- f. Exit Specific Mass Flow and Enthalpy Rise,
 $100\%N/\sqrt{\theta}$

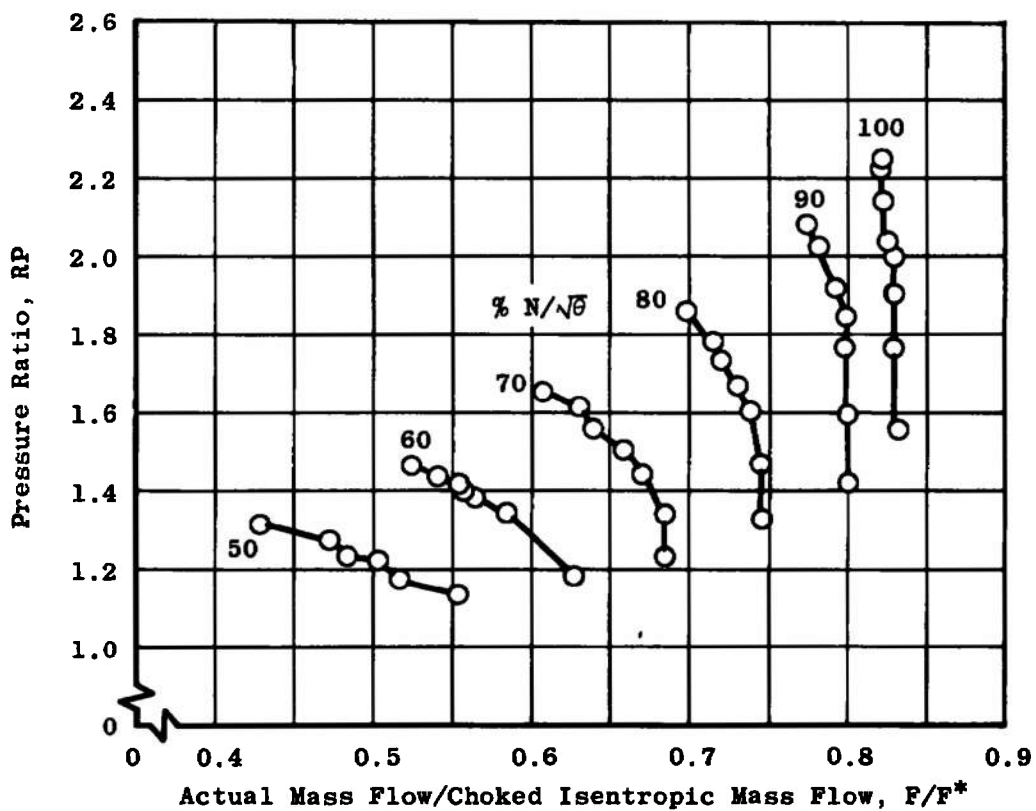
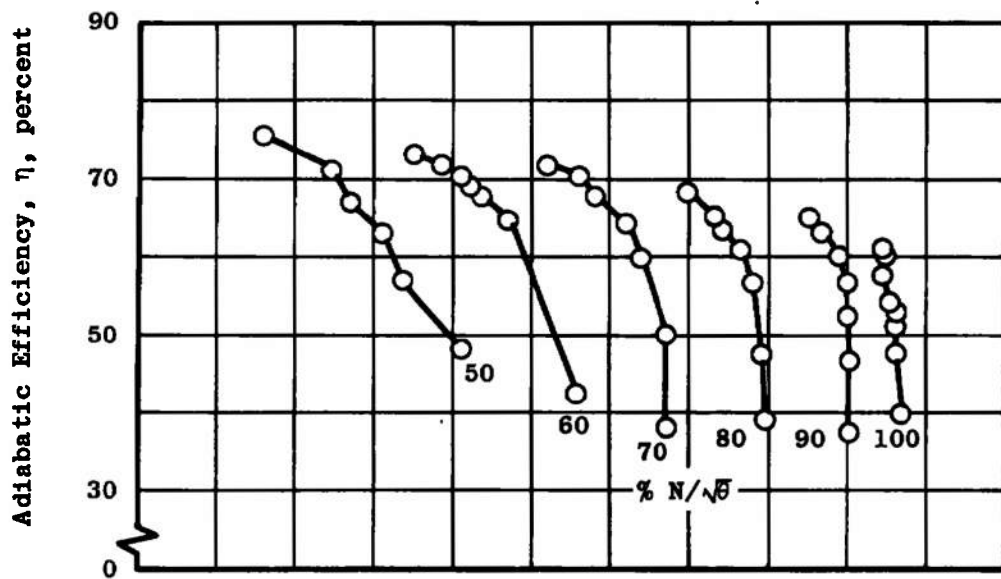
TABLES

V-1 Configuration R2C1

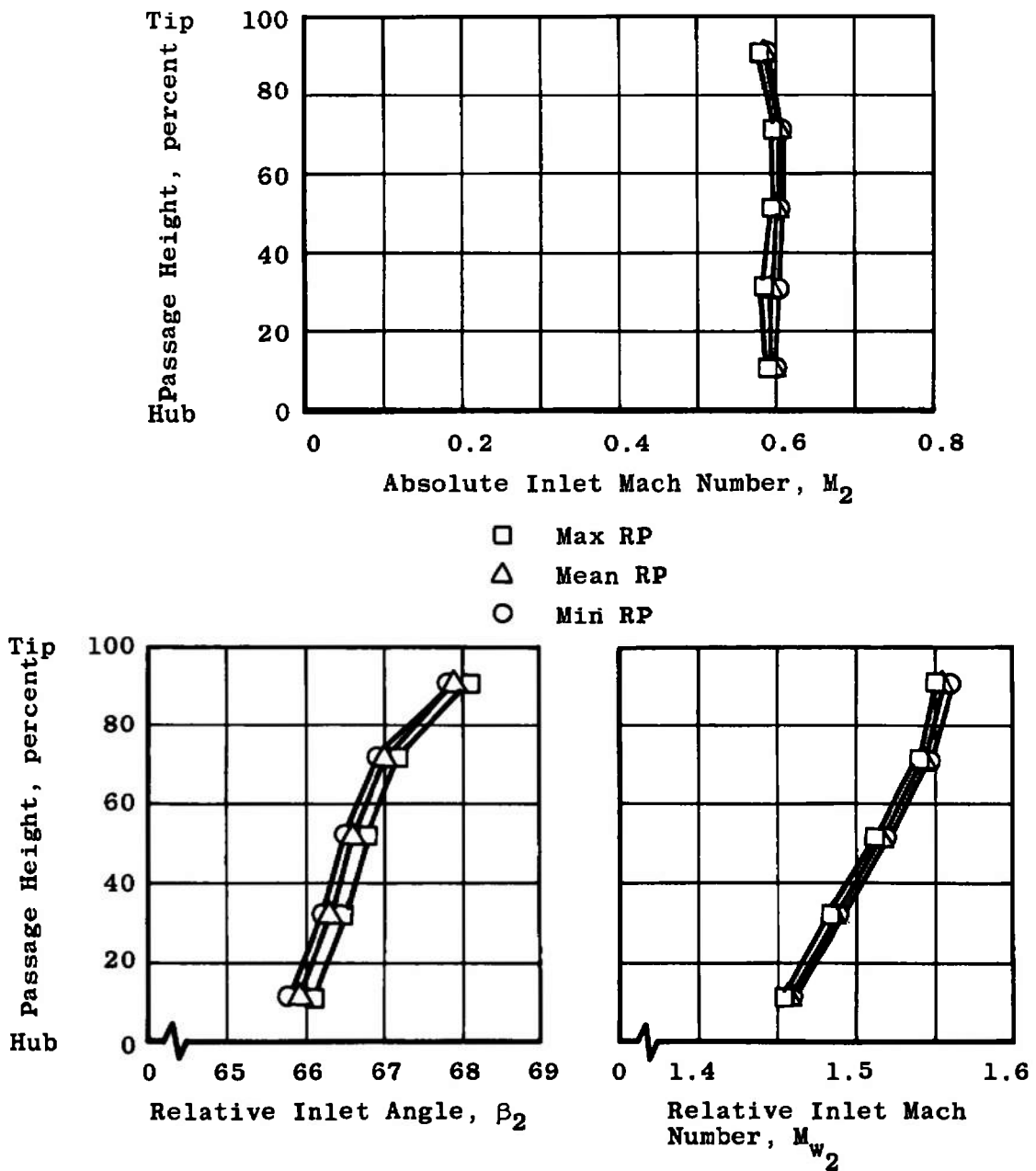
V-11 Configuration R2C2



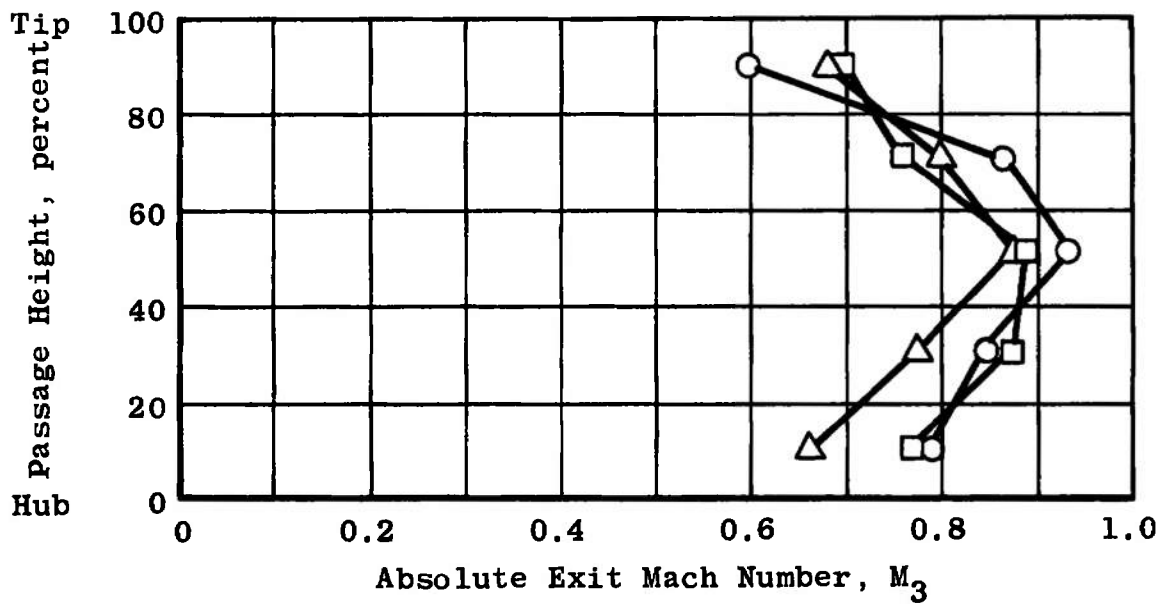
a. Compressor Performance Characteristics Based on Equivalent Weight Flow
Fig. V-1 Configuration R2C1



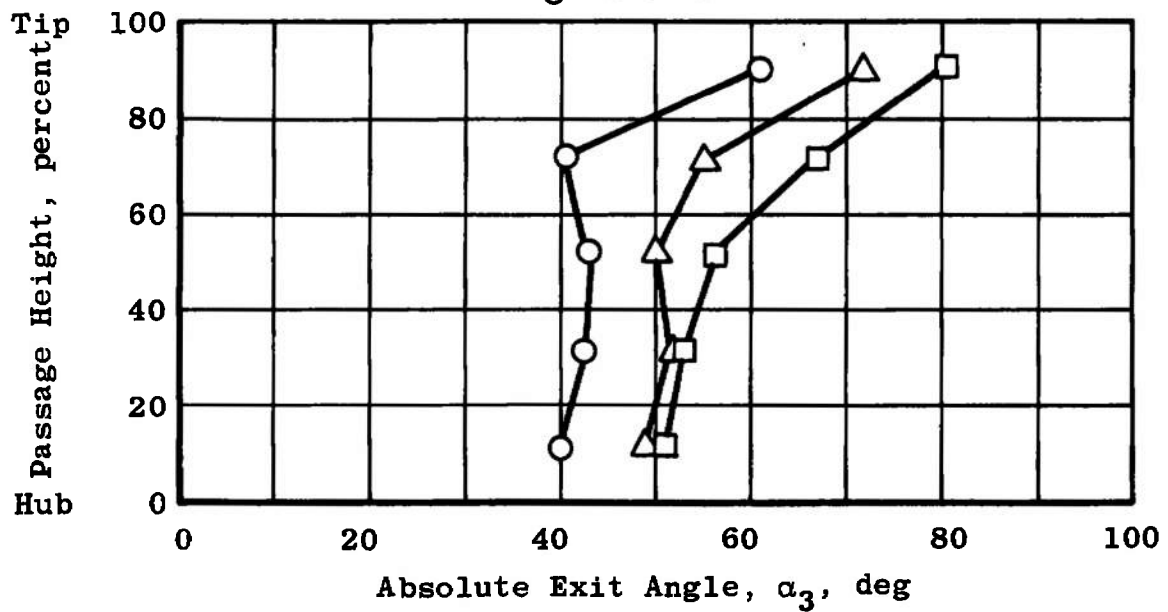
b. Compressor Performance Characteristics Based on Weight Flow Ratio
Fig. V-1 Continued



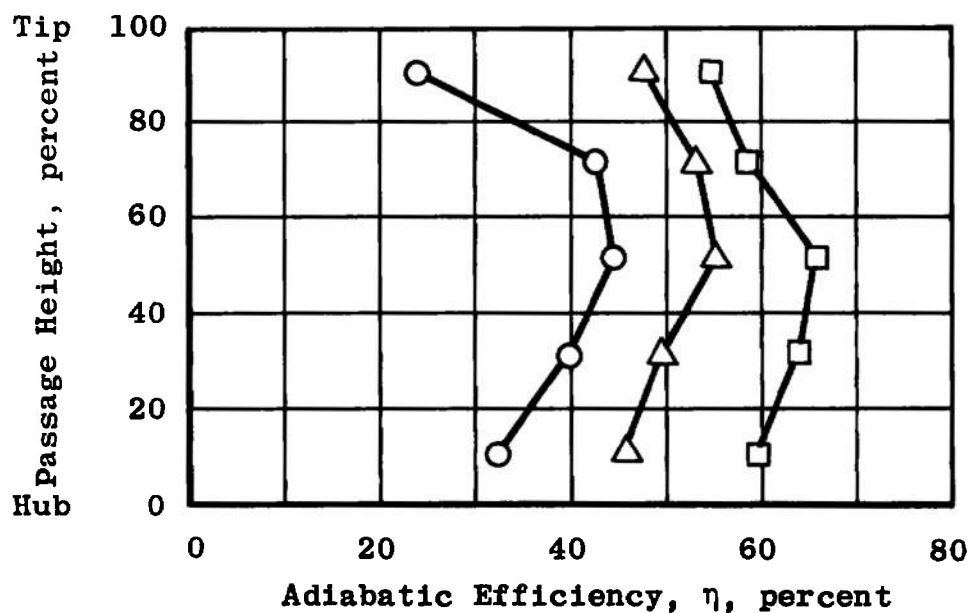
c. Inlet Parameters, $100\%N/\sqrt{\theta}$
Fig. V-1 Continued



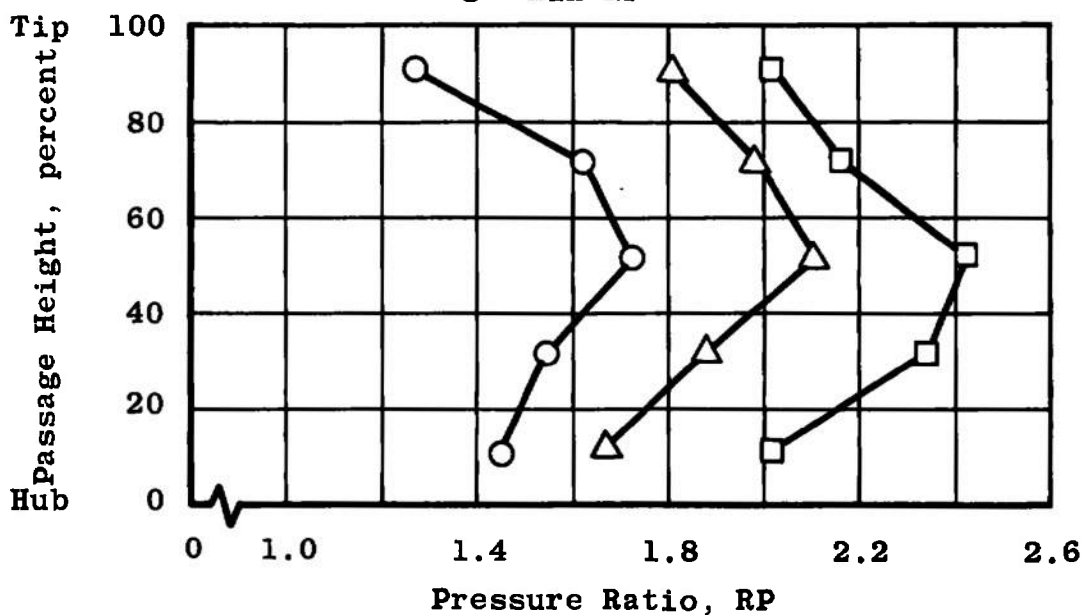
□ Max RP
 △ Mean RP
 ○ Min RP



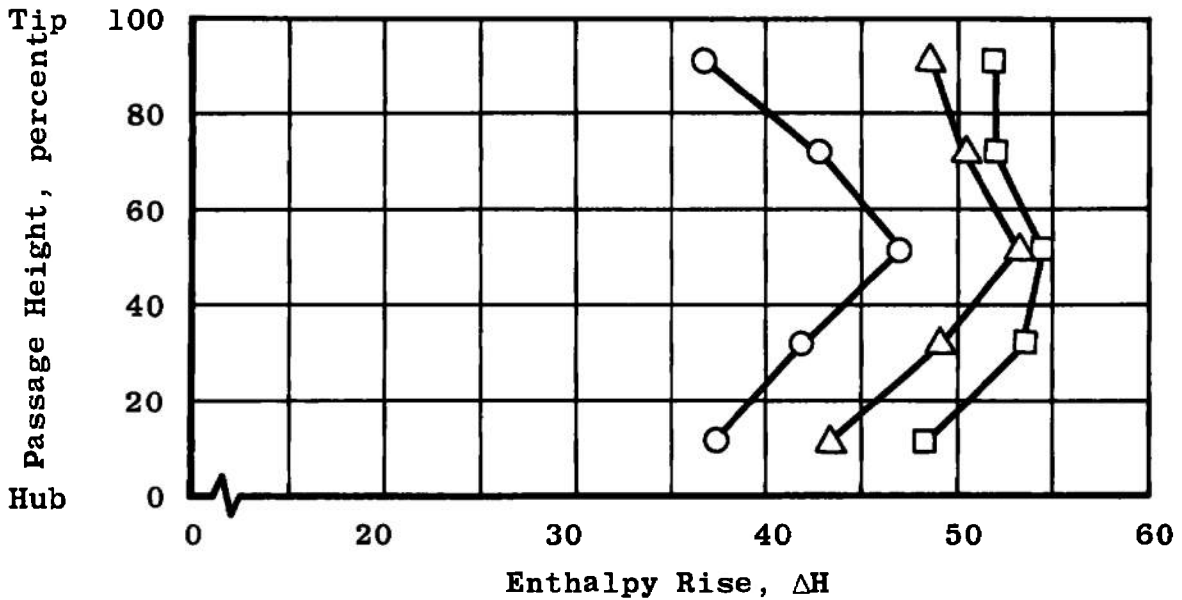
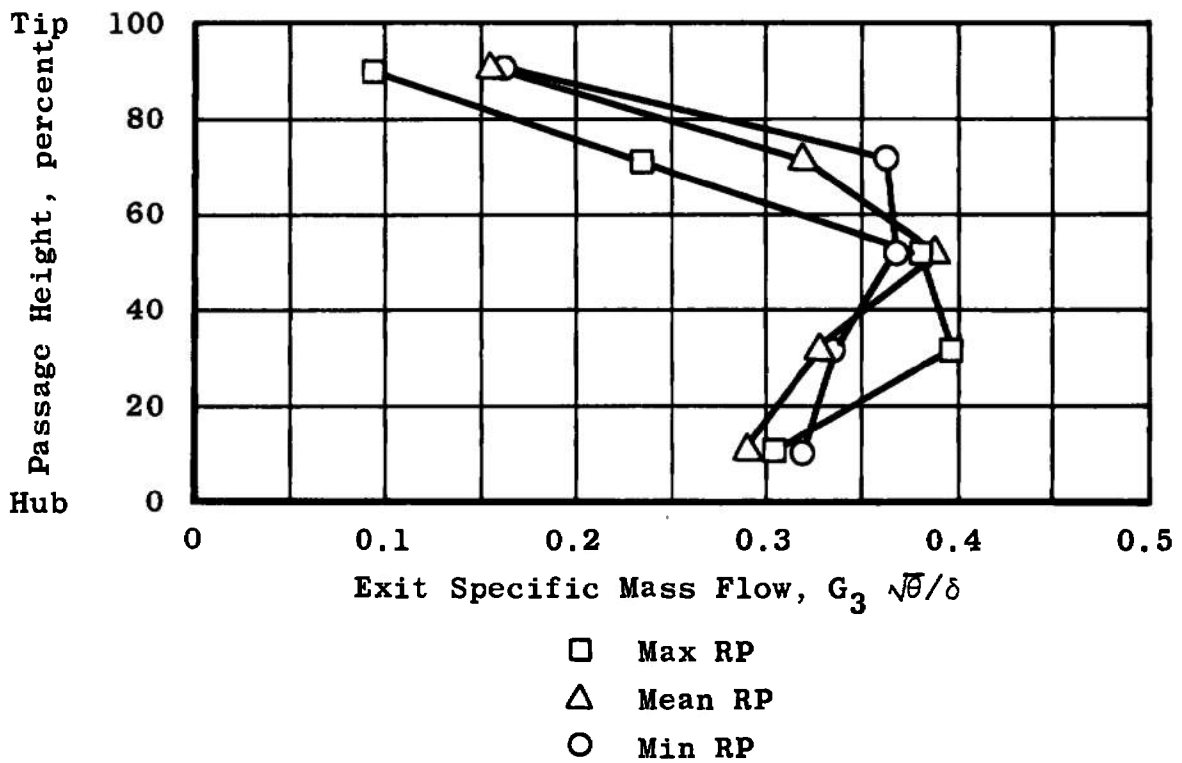
d. Exit Parameters, $100\%N/\sqrt{\theta}$
 Fig. V-1 Continued



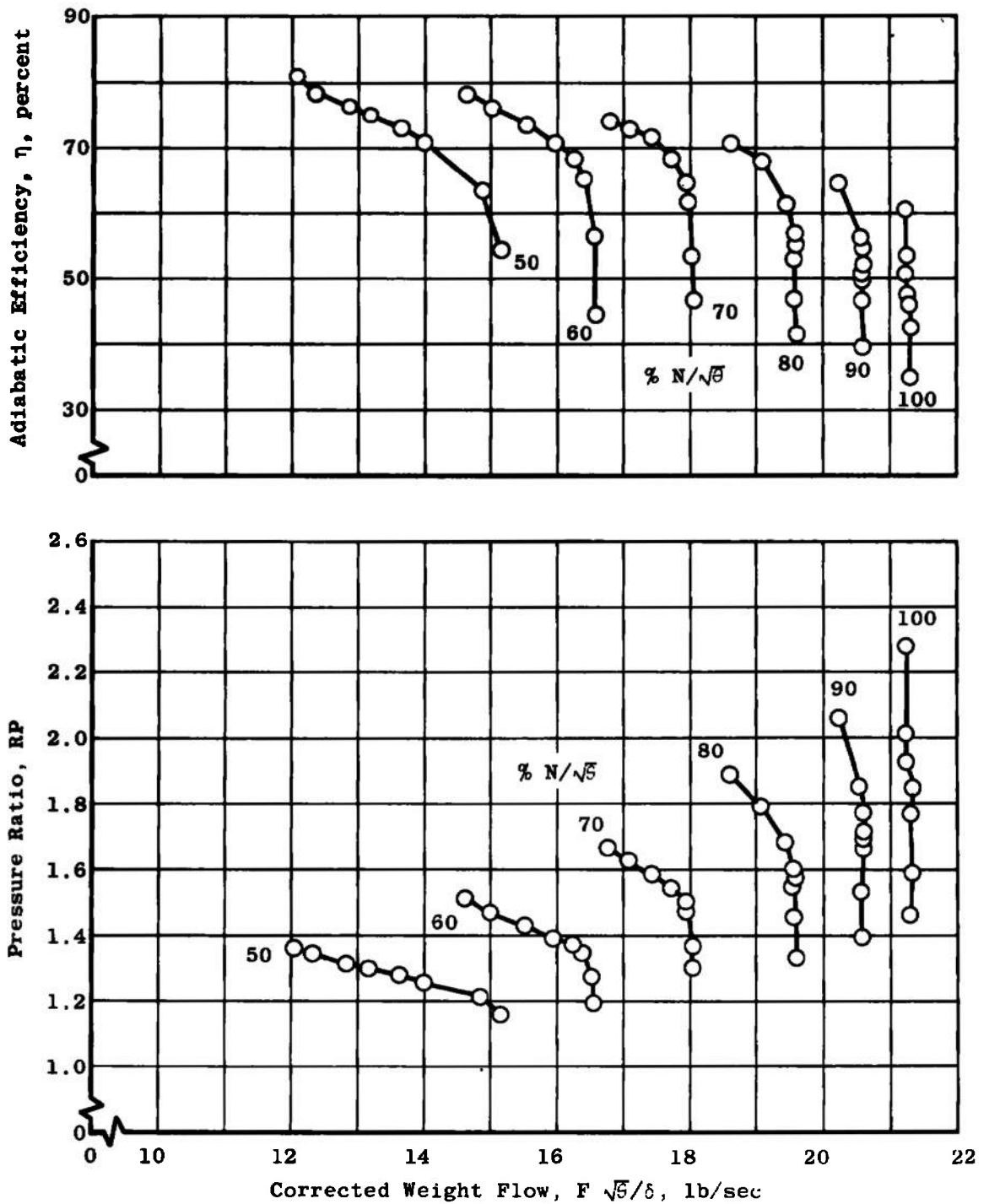
□ Max RP
 △ Mean RP
 ○ Min RP



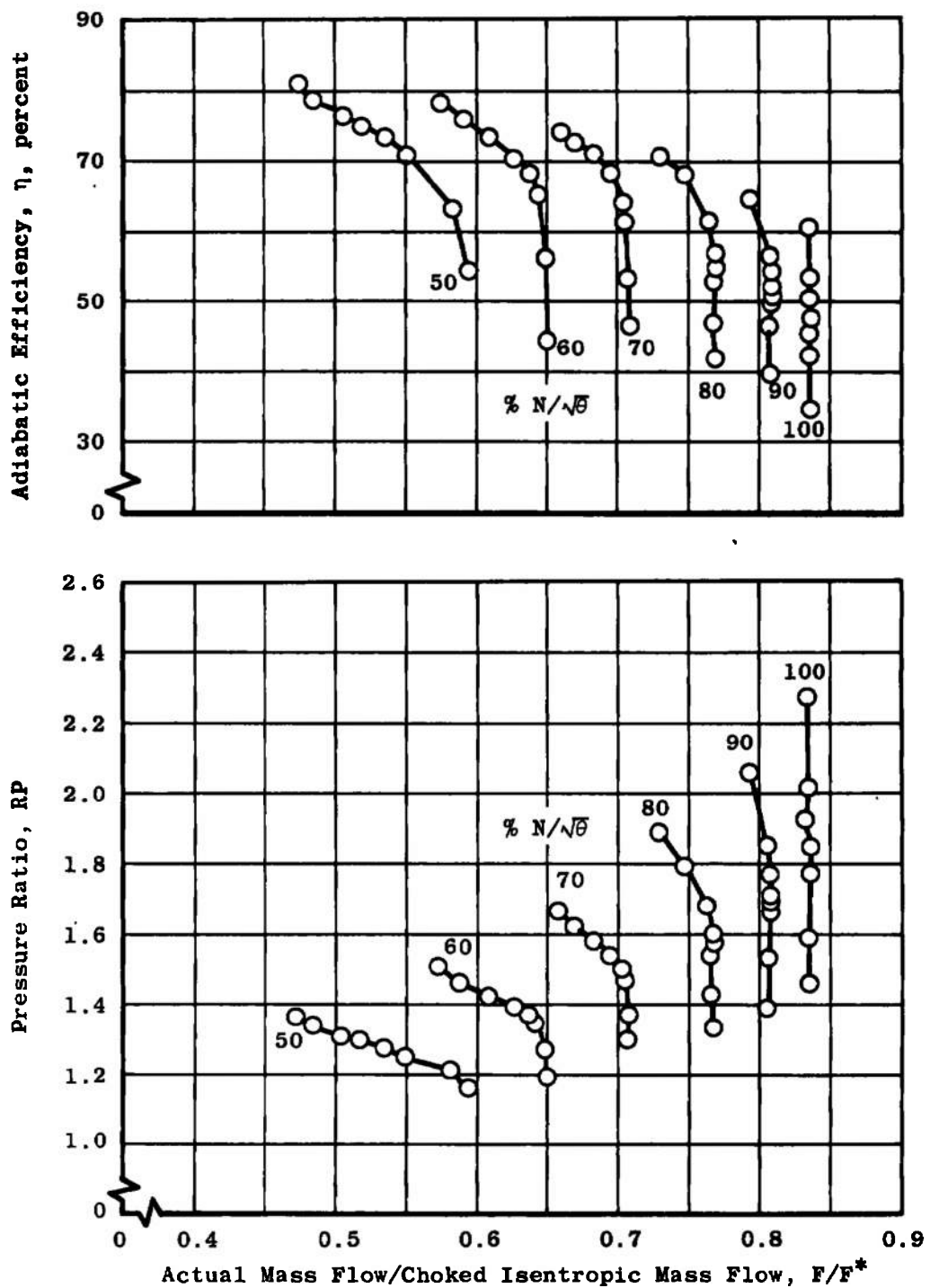
e. Adiabatic Efficiency and Pressure Ratio, $100\%N/\sqrt{\theta}$
 Fig. V-1 Continued



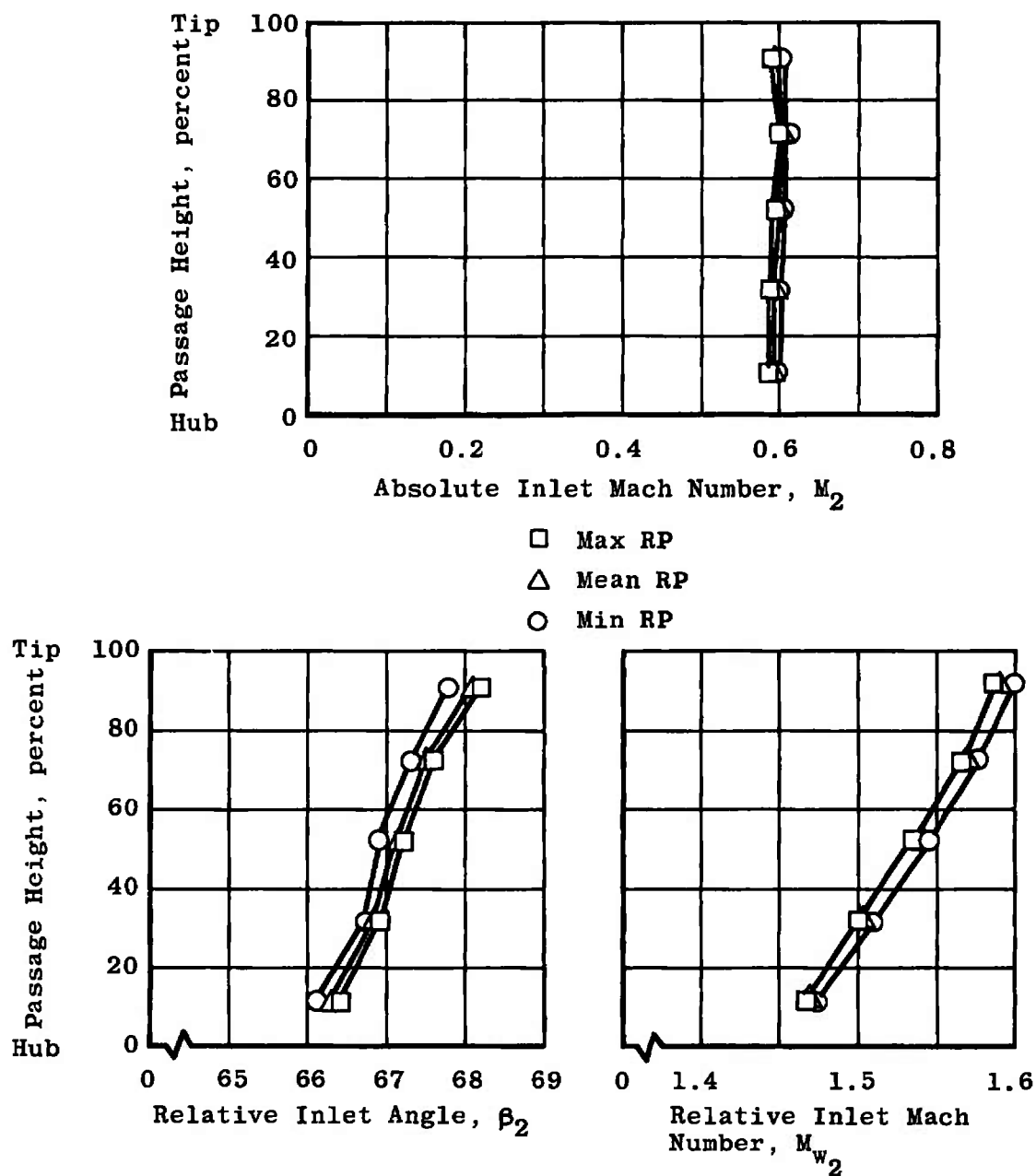
f. Exit Specific Mass Flow and Enthalpy Rise, 100%N/ $\sqrt{\theta}$
 Fig. V-1 Concluded



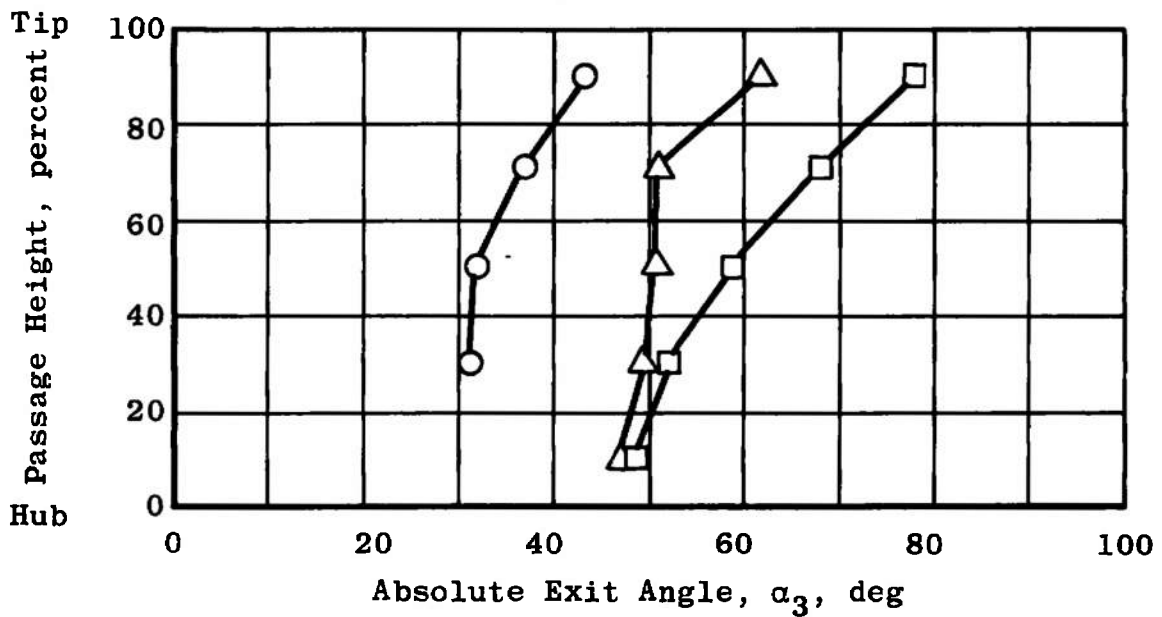
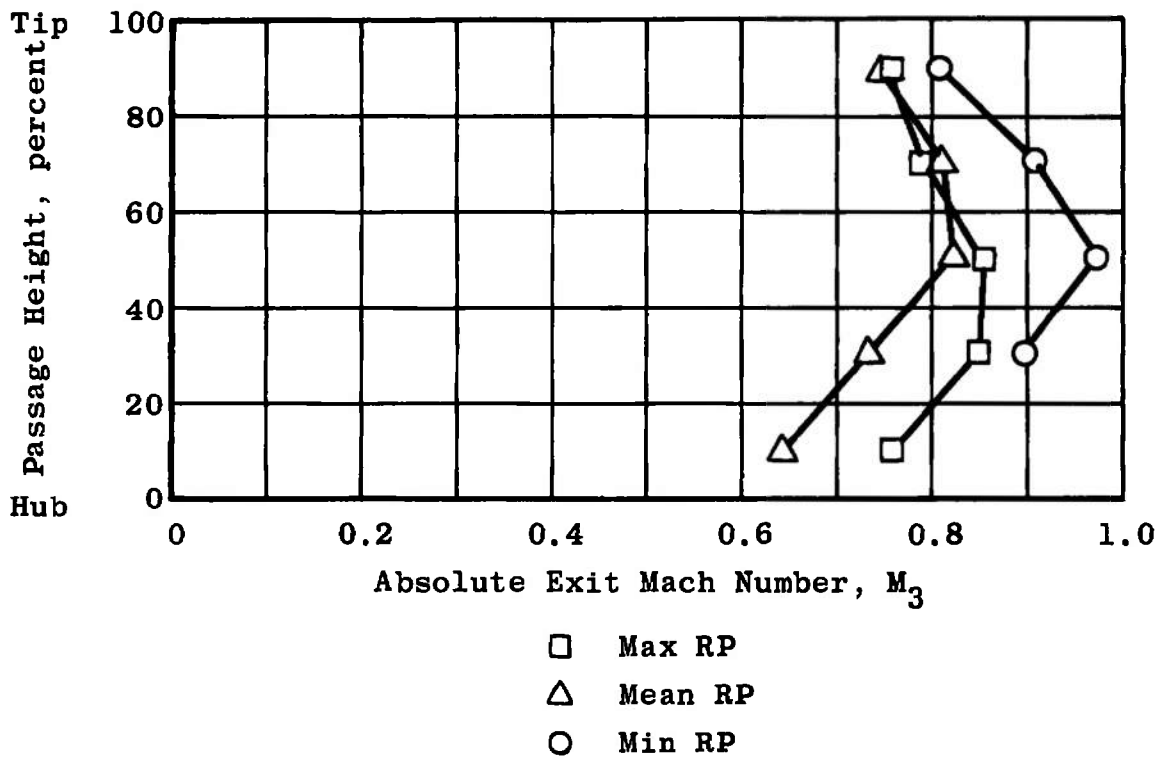
a. Compressor Performance Characteristics Based on Equivalent Weight Flow
Fig. V-2 Configuration R2C2



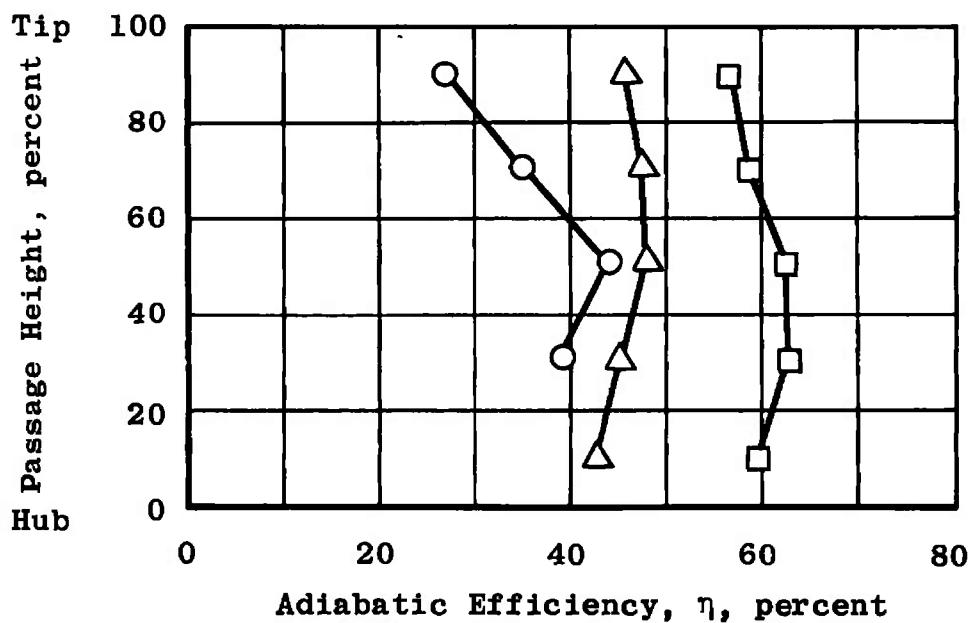
b. Compressor Performance Characteristics Based on Weight Flow Ratio
Fig. V-2 Continued



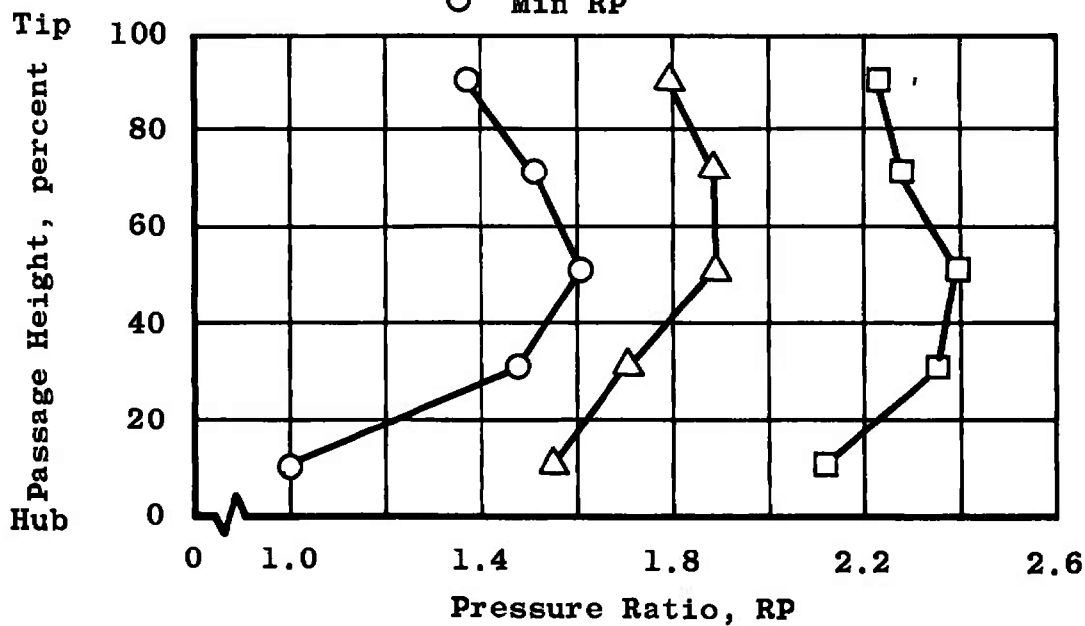
c. Inlet Performance, $100\%N/\sqrt{\theta}$
Fig. V-2 Continued



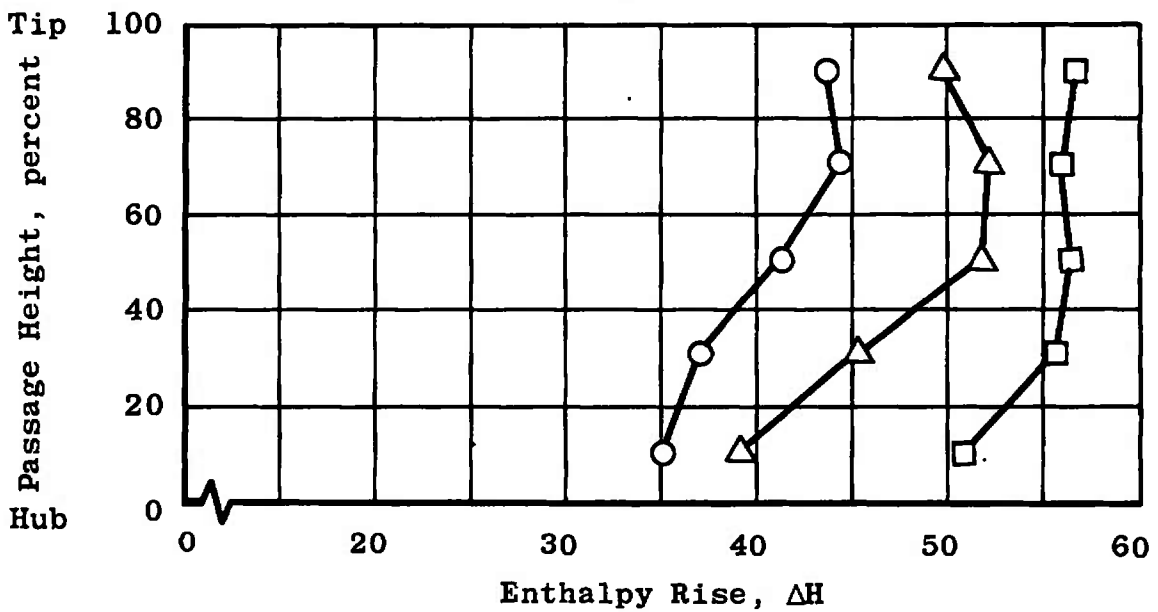
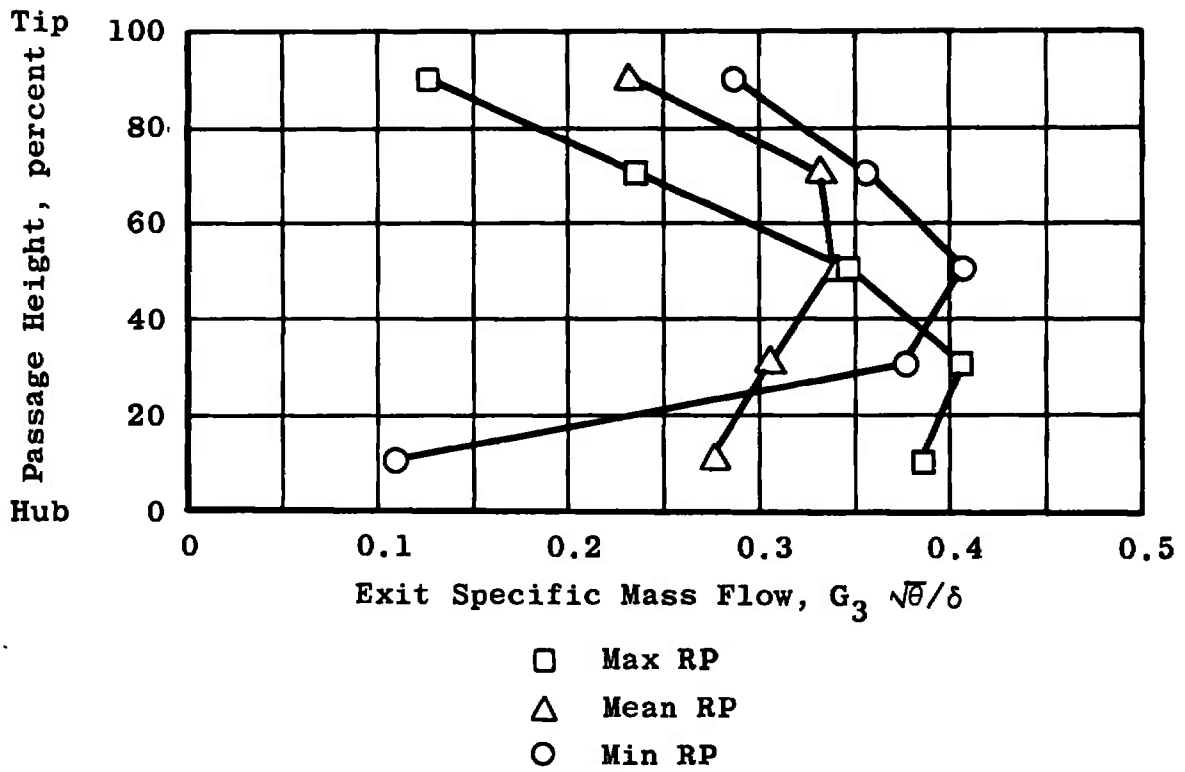
d. Exit Parameters, $100\%N/\sqrt{\theta}$
 Fig. V-2 Continued



□ Max RP
 △ Mean RP
 ○ Min RP



e. Adiabatic Efficiency and Pressure Ratio, $100N/\sqrt{\theta}$
 Fig. V-2 Continued



f. Exit Specific Mass Flow and Enthalpy Rise, 100%N/ $\sqrt{\theta}$
Fig. V-2 Concluded

TABLE V-I
CONFIGURATION R2C1

Pressure Ratio		M_2	β_2 , deg	M_{w2}	η , percent	RP	M_3	α_3 , deg	$G_3 \frac{\sqrt{\theta}}{\delta}$	$\Delta H/\theta$
100% N										
Maximum	1	0.579	68.1	1.551	54.7	2.06	0.691	80.0	0.093	52.0
	2	0.598	67.2	1.540	58.7	2.16	0.758	66.5	0.234	52.0
	3	0.595	66.8	1.512	65.5	2.42	0.889	56.2	0.381	54.5
	4	0.592	66.5	1.483	63.8	2.34	0.872	53.0	0.398	53.6
	5	0.589	66.1	1.454	59.8	2.07	0.769	51.0	0.304	48.2
Mean	1	0.585	67.9	1.556	47.5	1.81	0.688	71.1	0.155	48.5
	2	0.604	67.0	1.543	53.0	1.98	0.796	54.8	0.318	50.5
	3	0.601	66.6	1.516	55.3	2.11	0.873	50.0	0.384	53.4
	4	0.598	66.3	1.486	49.8	1.88	0.773	51.2	0.326	49.2
	5	0.596	65.9	1.456	45.4	1.67	0.663	48.8	0.290	43.3
Minimum	1	0.588	67.9	1.560	23.9	1.27	0.596	60.4	0.158	36.8
	2	0.607	66.9	1.547	42.9	1.62	0.866	40.0	0.361	42.6
	3	0.605	66.5	1.519	44.3	1.72	0.931	43.0	0.367	47.0
	4	0.602	66.2	1.489	39.6	1.55	0.842	42.5	0.332	42.0
	5	0.599	65.8	1.460	37.1	1.45	0.783	40.0	0.320	37.5
90% N										
Maximum	1	0.511	68.7	1.406	59.6	2.00	0.679	73.5	0.150	45.6
	2	0.542	67.3	1.402	63.9	2.12	0.760	63.0	0.267	46.6
	3	0.548	66.6	1.381	67.9	2.24	0.831	58.0	0.338	47.4
	4	0.551	66.1	1.358	66.1	2.09	0.781	55.0	0.339	44.3
	5	0.558	65.3	1.336	64.5	1.91	0.700	53.0	0.315	39.2
Mean	1	0.552	67.3	1.429	50.1	1.71	0.656	64.5	0.194	41.4
	2	0.572	66.2	1.419	55.2	1.86	0.762	52.5	0.317	43.6
	3	0.571	65.8	1.394	56.2	1.91	0.806	52.4	0.332	45.1
	4	0.569	65.4	1.368	52.1	1.74	0.721	52.1	0.294	40.7
	5	0.569	64.9	1.342	46.6	1.55	0.610	48.5	0.264	35.7
Minimum	1	0.554	67.3	1.432	35.2	1.36	0.655	46.5	0.254	32.8
	2	0.576	66.1	1.423	39.8	1.50	0.768	39.5	0.330	38.1
	3	0.576	65.7	1.399	40.3	1.52	0.796	44.7	0.311	39.3
	4	0.575	65.2	1.372	36.6	1.40	0.719	43.0	0.288	34.1
	5	0.574	64.7	1.347	30.8	1.27	0.621	39.5	0.261	28.7

TABLE V-I (Continued)

Pressure Ratio		M_2	β_2 , deg	M_{w2}	η , percent	RP	M_3	α_3 , deg	$G_3 \frac{\sqrt{\theta}}{\delta}$	$\Delta H/\theta$
80% N										
Maximum	1	0.436	64.2	1.229	65.5	1.87	0.649	67.5	0.189	37.0
	2	0.461	67.8	1.222	68.1	1.93	0.702	62.2	0.248	37.8
	3	0.466	67.2	1.203	70.4	1.95	0.726	59.0	0.282	37.2
	4	0.472	66.5	1.185	69.2	1.85	0.678	57.0	0.275	34.5
	5	0.478	65.8	1.166	67.3	1.62	0.503	55.6	0.252	30.8
Mean	1	0.491	67.1	1.262	54.1	1.57	0.597	56.4	0.223	31.5
	2	0.508	66.0	1.253	58.3	1.66	0.681	50.7	0.290	33.4
	3	0.509	65.6	1.231	59.0	1.69	0.710	52.8	0.286	34.2
	4	0.513	65.0	1.211	56.1	1.58	0.643	52.4	0.259	31.0
	5	0.516	64.3	1.190	54.1	1.46	0.556	48.6	0.242	26.3
Minimum	1	0.427	66.9	1.264	37.8	1.31	0.601	45.0	0.244	26.7
	2	0.515	65.8	1.254	40.9	1.38	0.665	42.9	0.278	29.0
	3	0.516	65.3	1.233	42.2	1.41	0.699	44.4	0.283	30.2
	4	0.518	64.7	1.212	38.5	1.32	0.630	42.3	0.263	26.4
	5	0.519	64.2	1.191	33.7	1.22	0.543	39.5	0.236	21.8
70% N										
Maximum	1	0.366	69.9	1.067	68.0	1.65	0.576	66.0	0.171	28.1
	2	0.389	68.5	1.061	71.3	1.70	0.626	61.8	0.215	28.6
	3	0.395	67.8	1.046	74.3	1.72	0.650	58.5	0.245	28.0
	4	0.403	67.0	1.031	72.8	1.64	0.606	57.0	0.236	26.0
	5	0.411	66.1	1.015	70.7	1.54	0.535	56.5	0.210	23.2
Mean	1	0.428	67.0	1.097	53.9	1.42	0.532	55.9	0.195	22.9
	2	0.445	65.9	1.090	59.0	1.48	0.599	48.6	0.258	24.3
	3	0.446	65.4	1.071	65.2	1.50	0.624	50.0	0.260	24.4
	4	0.448	64.8	1.054	68.9	1.43	0.575	49.2	0.242	22.3
	5	0.450	64.2	1.035	60.5	1.35	0.505	44.5	0.231	19.0
Minimum	1	0.439	66.6	1.104	30.5	1.19	0.521	44.0	0.212	18.8
	2	0.456	65.4	1.096	40.6	1.26	0.600	39.6	0.259	21.1
	3	0.456	64.9	1.078	38.2	1.30	0.646	42.3	0.266	22.5
	4	0.459	64.3	1.060	41.0	1.23	0.590	40.0	0.250	20.0
	5	0.460	63.8	1.042	35.2	1.15	0.512	35.8	0.230	16.2

TABLE V-I (Continued)

Pressure Ratio		M_2	β_2 , deg	M_{w2}	η , percent	RP	M_3	α_3 , deg	$G_3 \sqrt{\frac{\theta}{\delta}}$	$\Delta H/\theta$
60% N										
Maximum	1	0.306	70.4	0.910	69.7	1.45	0.494	63.5	0.153	20.1
	2	0.328	68.8	0.905	73.2	1.49	0.538	58.6	0.194	20.4
	3	0.328	68.3	0.890	76.1	1.50	0.562	56.6	0.213	20.2
	4	0.336	67.4	0.876	74.9	1.46	0.528	55.4	0.205	18.9
	5	0.344	66.5	0.862	70.5	1.38	0.454	55.6	0.175	17.0
Mean	1	0.339	68.4	0.924	64.2	1.36	0.470	59.0	0.160	17.7
	2	0.361	66.9	0.919	69.6	1.41	0.534	51.6	0.219	18.4
	3	0.361	66.4	0.903	70.2	1.42	0.553	51.4	0.227	18.7
	4	0.367	65.6	0.890	68.4	1.37	0.511	50.8	0.216	17.2
	5	0.372	64.8	0.876	64.7	1.30	0.439	49.1	0.187	15.0
Minimum	1	0.398	65.3	0.952	36.6	1.14	0.434	42.0	0.1854	12.8
	2	0.417	63.9	0.947	45.7	1.20	0.528	36.0	0.2451	14.8
	3	0.414	63.5	0.930	48.1	1.23	0.564	41.6	0.241	15.6
	4	0.416	62.9	0.915	43.3	1.18	0.517	41.8	0.219	14.1
	5	0.416	62.4	0.898	31.0	1.10	0.412	35.7	0.189	11.2
50% N										
Maximum	1	0.248	70.8	0.755	71.6	1.30	0.417	64.8	0.118	13.8
	2	0.261	69.6	0.747	75.2	1.33	0.451	59.5	0.152	13.9
	3	0.262	69.1	0.735	78.8	1.34	0.470	56.7	0.170	13.6
	4	0.267	68.3	0.723	77.8	1.31	0.448	55.2	0.168	12.9
	5	0.272	67.5	0.710	72.6	1.26	0.393	55.0	0.147	11.9
Mean	1	0.304	67.0	0.778	59.1	1.19	0.390	51.2	0.152	11.0
	2	0.314	65.9	0.770	66.0	1.23	0.443	44.5	0.196	11.4
	3	0.311	65.7	0.756	66.8	1.24	0.464	46.0	0.199	11.7
	4	0.315	64.9	0.744	62.6	1.20	0.424	44.5	0.187	10.9
	5	0.316	64.4	0.731	58.4	1.16	0.364	42.4	0.166	9.4
Minimum	1	0.340	64.6	0.793	40.8	1.10	0.363	39.5	0.163	8.4
	2	0.352	63.4	0.786	50.6	1.14	0.442	35.2	0.211	9.7
	3	0.349	63.1	0.772	54.0	1.16	0.472	39.0	0.214	10.2
	4	0.350	62.5	0.760	49.2	1.13	0.434	36.6	0.202	9.2
	5	0.351	62.0	0.746	43.3	1.10	0.378	32.0	0.186	7.6

TABLE V-I (Continued)

Axial Distance, d		-2.0	-1.0	-0.25	0	0.1	0.3	0.5	0.7	0.9	1.1	1.35	1.6	2.1	2.6	3.1	4.1
100% N		Ratio of Wall Static Pressure to Inlet Total Pressure															
Maximum RP	OW	0.824	0.810	0.785	0.747	0.774	0.878	0.985	1.025	1.178	1.388	1.380	1.340	1.387	1.448	1.511	1.537
	1W	0.827	0.812	0.794								1.311	1.352	1.360	1.358	1.393	1.433
M Mean RP	OW	0.819	0.809	0.782	0.738	0.859	0.758	0.751	0.819	0.903	1.072	1.124	1.104	---	1.273	1.334	1.343
	1W	0.818	0.807	0.790								1.100	1.132	1.173	1.197	1.237	1.261
Minimum RP	OW	0.821	0.807	0.780	0.739	0.649	0.734	0.658	0.634	0.634	0.756	0.829	0.818	0.863	0.942	1.004	1.068
	1W	0.818	0.806	0.788								0.716	0.745	0.925	0.935	0.964	1.011
90% N																	
Maximum RP	OW	0.848	0.835	0.829	0.819	0.845	1.032	1.140	1.194	1.275	1.346	1.337	1.318	1.390	1.438	1.482	1.474
	1W	0.846	0.834	0.809								1.277	1.311	1.338	1.352	1.367	1.387
Mean RP	OW	0.838	0.825	0.803	0.772	0.728	0.810	0.789	0.835	0.909	1.049	1.094	1.089	1.199	1.259	1.297	1.279
	1W	0.834	0.825	0.805								1.088	1.121	1.160	1.180	1.198	1.214
Minimum RP	OW	0.836	0.824	0.801	0.772	0.772	0.779	0.719	0.688	0.645	0.713	0.826	0.832	0.923	1.013	1.030	1.017
	1W	0.833	0.822	0.802								0.787	0.826	0.938	0.983	0.976	0.982
80% N																	
Maximum RP	OW	0.881	0.874	0.872	0.877	0.869	1.056	1.185	1.216	1.254	1.303	1.318	1.323	---	1.410	1.417	1.405
	1W	0.884	0.874	0.855								1.287	1.290	1.324	1.328	1.334	1.335
Mean RP	OW	0.864	0.855	0.842	0.831	0.837	0.892	0.908	0.918	1.003	1.052	1.085	1.101	1.183	1.241	1.239	1.221
	1W	0.864	0.854	0.836								1.103	1.120	1.153	1.156	1.179	1.176
Minimum RP	OW	0.862	0.854	0.838	0.828	0.808	0.828	0.774	0.745	0.732	0.802	0.890	0.910	0.984	1.035	1.034	1.018
	1W	0.862	0.853	0.834								0.909	0.940	0.976	0.983	0.997	0.992

TABLE V-1 (Concluded)

Axial Distance, d		-2.0	-1.0	-0.25	0	0.1	0.3	0.5	0.7	0.9	1.1	1.35	1.6	2.1	2.6	3.1	4.1
70% N		Ratio of Wall Static Pressure to Inlet Total Pressure															
Maximum RP	OW	0.912	0.908	0.908	0.919	0.894	1.080	1.165	1.181	1.204	1.243	1.260	1.265	1.296	1.338	1.325	1.312
	IW	0.916	0.908	0.890								1.230	1.235	1.256	1.266	1.263	1.264
Mean RP	OW	0.892	0.886	0.876	0.866	0.879	0.928	0.934	0.955	0.996	1.023	1.047	1.059	1.137	1.172	1.173	1.161
	IW	0.894	0.885	0.872								1.057	1.083	1.106	1.129	1.130	1.128
Minimum RP	OW	0.889	0.881	0.869	0.858	0.842	0.797	0.730	0.704	0.741	0.817	0.870	0.866	0.938	0.997	0.997	0.986
	IW	0.889	0.880	0.866								0.894	0.920	0.935	0.964	0.962	0.981
60% N																	
Maximum RP	OW	0.935	0.933	0.936	0.945	0.929	1.072	1.126	1.135	1.151	1.176	1.193	1.195	1.202	1.236	1.234	1.227
	IW	0.937	0.932	0.921								1.171	1.172	1.190	1.189	1.194	1.193
Mean RP	OW	0.923	0.920	0.920	0.935	0.936	0.988	1.033	1.048	1.068	1.083	1.098	1.102	1.164	1.197	1.171	1.162
	IW	0.927	0.920	0.909								1.098	1.104	1.123	1.156	1.137	1.136
Minimum RP	OW	0.906	0.902	0.890	0.883	0.853	0.778	0.775	0.800	0.834	0.866	0.905	0.907	0.950	0.990	1.003	0.991
	IW	0.906	0.900	0.889								0.923	0.942	0.959	0.970	0.977	0.978
50% N																	
Maximum RP	OW	0.956	0.955	0.958	0.962	0.954	1.047	1.088	1.091	1.101	1.124	1.131	1.128	1.156	1.186	1.161	1.153
	IW	0.957	0.954	0.949								1.118	1.119	1.130	1.135	1.135	1.129
Mean RP	OW	0.938	0.935	0.936	0.938	0.945	0.960	0.968	0.978	0.990	1.000	1.012	1.018	1.065	1.085	1.078	1.068
	IW	0.942	0.938	0.933								1.024	1.033	1.045	1.062	1.059	1.053
Minimum RP	OW	0.929	0.925	0.920	0.910	0.882	0.871	0.860	0.875	0.890	0.919	0.937	0.937	0.985	1.005	1.006	0.999
	IW	0.931	0.926	0.919								0.954	0.971	0.980	0.993	0.992	0.988

TABLE V-II
CONFIGURATION R2C2

Pressure Ratio		M_2	β , deg	M_{w2}	η , percent	RP	M_3	α_3 , deg	$G_3 \frac{\sqrt{\theta}}{\delta}$	$\Delta H/\theta$
100% N										
Maximum	1	0.590	68.2	1.586	0.564	2.226	0.755	78.0	0.124	56.66
	2	0.599	67.6	1.567	0.586	2.269	0.788	68.0	0.233	55.94
	3	0.595	67.2	1.535	0.623	2.392	0.852	58.8	0.346	56.45
	4	0.588	66.9	1.501	0.625	2.353	0.849	52.0	0.406	55.06
	5	0.587	66.4	1.467	0.594	2.118	0.757	48.5	0.385	50.08
Mean	1	0.593	68.1	1.588	0.453	1.790	0.744	61.7	0.231	49.72
	2	0.601	67.5	1.568	0.471	1.879	0.808	51.0	0.330	52.15
	3	0.598	67.1	1.536	0.476	1.884	0.824	50.2	0.339	51.76
	4	0.592	66.8	1.502	0.450	1.702	0.734	49.1	0.306	45.30
	5	0.590	66.3	1.466	0.422	1.546	0.641	47.0	0.276	39.03
Minimum	1	0.603	67.8	1.599	0.265	1.365	0.806	43.0	0.285	43.59
	2	0.609	67.3	1.577	0.346	1.504	0.906	36.5	0.354	44.43
	3	0.605	66.9	1.545	0.435	1.603	0.971	31.7	0.407	41.32
	4	0.599	66.7	1.510	0.389	1.467	0.899	31.0	0.376	37.01
	5	0.596	66.1	1.474	-0.002	0.998	0.464	60.0	0.108	30.52
90% N										
Maximum	1	0.547	67.6	1.433	0.595	1.997	0.680	74.0	0.146	45.7
	2	0.558	66.8	1.418	0.608	2.023	0.708	65.0	0.231	45.6
	3	0.555	66.5	1.389	0.655	2.132	0.778	57.0	0.326	45.8
	4	0.552	66.1	1.361	0.667	2.128	0.789	51.4	0.375	44.9
	5	0.553	65.5	1.331	0.659	1.960	0.717	48.9	0.356	40.0
Mean	1	0.562	67.0	1.441	0.487	1.672	0.679	61.9	0.212	40.4
	2	0.571	66.3	1.424	0.509	1.747	0.744	49.8	0.314	42.2
	3	0.568	66.0	1.395	0.516	1.760	0.766	48.5	0.329	42.3
	4	0.564	65.6	1.365	0.486	1.603	0.680	48.0	0.292	36.9
	5	0.563	65.1	1.334	0.464	1.471	0.595	46.7	0.259	31.3
Minimum	1	0.569	66.9	1.450	0.391	1.383	0.642	44.4	0.266	30.9
	2	0.577	66.2	1.431	0.429	1.459	0.716	37.5	0.326	33.0
	3	0.574	65.8	1.403	0.427	1.480	0.744	41.8	0.315	34.6
	4	0.571	65.5	1.373	0.376	1.359	0.661	41.6	0.278	30.3
	5	0.569	64.9	1.341	0.318	1.250	0.571	39.4	0.246	25.7

TABLE V-II (Continued)

Pressure Ratio		M_2	β , deg	M_{w2}	η , percent	RP	M_3	α_3 , deg	$G_3 \sqrt{\frac{\theta}{\delta}}$	$\Delta H/\theta$
80% N										
Maximum	1	0.465	68.5	1.264	0.623	1.816	0.633	71.9	0.148	37.1
	2	0.481	67.4	1.253	0.685	1.921	0.712	63.9	0.235	37.2
	3	0.484	66.8	1.230	0.748	2.012	0.774	57.5	0.311	36.7
	4	0.485	66.3	1.206	0.723	1.914	0.734	53.0	0.326	35.0
	5	0.492	65.4	1.184	0.702	1.756	0.651	50.7	0.301	30.9
Mean	1	0.521	66.2	1.293	0.513	1.550	0.639	63.6	0.184	32.3
	2	0.530	65.5	1.277	0.543	1.606	0.695	48.6	0.295	33.2
	3	0.528	65.1	1.252	0.565	1.625	0.721	47.1	0.313	32.7
	4	0.523	64.7	1.226	0.511	1.497	0.641	46.5	0.278	29.7
	5	0.523	64.1	1.200	0.482	1.383	0.556	44.25	0.249	25.0
Minimum	1	0.522	66.3	1.295	0.401	1.383	0.610	44.1	0.252	25.8
	2	0.532	65.5	1.281	0.445	1.388	0.678	40.8	0.294	27.5
	3	0.530	65.0	1.256	0.462	1.398	0.696	41.2	0.299	27.1
	4	0.526	64.7	1.230	0.402	1.300	0.619	38.2	0.275	24.1
	5	0.524	64.1	1.204	0.322	1.191	0.513	37.2	0.230	19.8
70% N										
Maximum	1	0.407	68.2	1.096	68.39	1.652	0.579	68.4	0.1553	28.05
	2	0.419	67.3	1.084	72.77	1.701	0.627	61.4	0.2183	28.00
	3	0.423	66.6	1.066	76.87	1.723	0.655	56.0	0.2650	27.20
	4	0.424	66.1	1.046	76.12	1.669	0.628	52.8	0.2728	25.73
	5	0.430	65.3	1.026	74.36	1.568	0.561	52.5	0.2432	22.94
Mean	1	0.460	65.8	1.122	56.67	1.451	0.567	65.7	0.1523	24.62
	2	0.466	65.1	1.108	62.26	1.513	0.631	50.8	0.2598	25.09
	3	0.463	64.7	1.086	65.88	1.529	0.654	47.5	0.2868	24.35
	4	0.459	64.4	1.063	62.38	1.461	0.609	45.0	0.2769	22.79
	5	0.458	63.9	1.040	57.91	1.355	0.519	42.2	0.2456	19.45
Minimum	1	0.456	66.0	1.122	44.81	1.289	0.558	48.3	0.2192	20.87
	2	0.467	65.1	1.110	50.13	1.347	0.626	41.3	0.2764	22.06
	3	0.467	64.6	1.090	51.67	1.366	0.653	43.0	0.2789	22.45
	4	0.465	64.2	1.069	44.03	1.278	0.580	41.4	0.2514	20.49
	5	0.467	63.5	1.048	38.46	1.190	0.492	38.0	0.2231	16.96

TABLE V-II (Continued)

Pressure Ratio		M ₂	β_2 , deg	M _{w2}	η , percent	RP	M ₃	α_3 , deg	$G_3 \sqrt{\frac{\theta}{\delta}}$	$\Delta H/\theta$
60% N										
Maximum	1	0.336	69.00	0.937	72.32	1.507	0.527	67.9	0.1393	21.37
	2	0.344	68.21	0.926	77.31	1.544	0.570	60.5	0.1969	21.26
	3	0.346	67.64	0.908	82.27	1.552	0.586	55.6	0.2317	20.22
	4	0.397	67.10	0.891	80.62	1.508	0.557	53.7	0.2293	19.20
	5	0.357	65.98	0.876	76.53	1.430	0.492	54.5	0.1971	17.49
Mean	1	0.403	65.40	0.968	58.67	1.325	0.483	57.4	0.1670	17.75
	2	0.408	64.72	0.956	64.61	1.372	0.542	47.5	0.2347	18.18
	3	0.406	64.30	0.937	69.09	1.380	0.559	45.6	0.2503	17.35
	4	0.403	63.96	0.918	67.47	1.344	0.532	42.7	0.2486	16.26
	5	0.407	63.12	0.901	64.54	0.283	0.471	42.1	0.2214	14.22
Minimum	1	0.408	65.04	0.968	38.63	1.170	0.490	48.0	0.1871	14.77
	2	0.414	64.33	0.955	48.91	1.228	0.567	36.8	0.2589	15.37
	3	0.413	63.85	0.937	51.16	1.242	0.588	37.0	0.2671	15.50
	4	0.410	63.51	0.918	43.23	1.187	0.534	36.6	0.2422	14.45
	5	0.416	62.62	0.903	33.38	1.114	0.445	35.5	0.2039	11.66
50% N										
Maximum	1	0.274	69.6	0.785	0.879	1.361	0.456	67.2	0.120	13.01
	2	0.278	68.9	0.773	0.790	1.378	0.484	60.0	0.163	15.09
	3	0.282	68.2	0.760	0.824	1.377	0.493	55.4	0.188	14.45
	4	0.286	67.5	0.746	0.805	1.353	0.474	53.7	0.187	13.93
	5	0.290	66.7	0.732	0.772	1.305	0.425	54.3	0.164	12.72
Mean	1	0.334	65.6	0.809	64.2	1.242	0.420	55.1	0.152	12.38
	2	0.340	64.8	0.799	69.2	1.269	0.462	47.1	0.199	12.65
	3	0.339	64.4	0.784	75.1	1.277	0.477	45.2	0.213	11.97
	4	0.335	64.1	0.767	73.7	1.257	0.458	41.7	0.216	11.38
	5	0.337	63.4	0.753	70.6	1.217	0.409	43.2	0.187	10.14
Minimum	1	0.381	62.8	0.832	0.490	1.126	0.400	45.0	0.166	8.78
	2	0.383	62.2	0.821	0.527	1.171	0.472	36.7	0.221	10.90
	3	0.380	61.8	0.804	0.586	0.189	0.501	37.0	0.234	10.75
	4	0.376	61.5	0.788	0.553	1.166	0.477	35.1	0.227	10.10
	5	0.373	61.1	0.772	0.543	1.132	0.435	32.1	0.214	8.27

TABLE V-II (Continued)

Axial Distance, d		-2.0	-1.0	-0.25	0	0.1	0.3	0.5	0.7	0.9	1.1	1.35	1.6	2.1	2.6	3.1	4.1
100% N		Ratio of Wall Static Pressure to Inlet Total Pressure															
Maximum RP	OW	0.815	0.804	0.783	0.734	0.696	0.827	0.894	1.048	1.203	1.370	1.421	1.426	1.418	1.495	1.539	1.578
	IW	0.821	0.811	0.795								1.357	1.384	---	1.369	1.441	1.465
Mean RP	OW	0.814	0.803	0.782	0.731	0.632	0.708	0.634	0.671	0.843	0.939	1.002	1.023	1.110	1.194	1.251	1.258
	IW	0.815	0.805	0.793								0.967	1.018	---	1.128	1.165	1.194
Minimum RP	OW	0.810	0.799	0.776	0.727	0.628	0.709	0.611	0.553	0.485	0.451	0.559	0.647	0.784	0.841	0.895	0.937
	IW	0.814	0.804	0.789								0.640	0.606	---	0.761	0.858	0.929
90% N																	
Maximum RP	OW	0.834	0.825	0.811	0.788	0.815	0.902	0.964	1.037	1.165	1.322	1.355	1.356	1.363	1.428	1.477	1.482
	IW	0.844	0.832	0.814								1.285	1.306	---	1.330	1.384	1.397
Mean RP	OW	0.831	0.821	0.802	0.762	0.699	0.752	0.691	0.710	0.840	0.945	1.010	1.032	1.109	1.182	1.239	1.228
	IW	0.831	0.821	0.808								1.000	1.045	---	1.115	1.150	1.168
Minimum RP	OW	0.826	0.817	0.797	0.759	0.693	0.749	0.683	0.591	0.671	0.788	0.837	0.852	0.943	1.015	1.055	1.046
	IW	0.831	0.821	0.805								0.825	0.890	---	0.966	0.997	1.010
80% N																	
Maximum RP	OW	0.856	0.860	0.858	0.854	0.880	1.005	1.075	1.121	1.192	1.290	1.296	1.306	1.322	1.371	1.397	1.404
	IW	0.876	0.870	0.849								1.247	1.265	---	1.293	1.313	1.330
Mean RP	OW	0.848	0.841	0.825	0.805	0.775	0.801	0.741	0.753	0.855	0.957	0.999	1.012	1.089	1.137	1.186	1.185
	IW	0.854	0.847	0.832								0.936	1.026	---	1.092	1.114	1.135
Minimum RP	OW	0.846	0.839	0.825	0.804	0.770	0.792	0.711	0.660	0.732	0.815	0.863	0.883	0.986	1.020	1.034	1.025
	IW	0.854	0.847	0.830								0.873	0.906	---	0.981	0.991	1.000

TABLE V-II (Concluded)

Axial Distance, d		-2.0	-1.0	-0.25	0	0.1	0.3	0.5	0.7	0.9	1.1	1.35	1.6	2.1	2.6	3.1	4.1
70% N		Ratio of Wall Static Pressure to Inlet Total Pressure															
Maximum RP	OW	0.897	0.893	0.890	0.902	0.905	1.011	1.080	1.125	1.168	1.236	1.259	1.279	1.284	1.315	1.325	1.320
	1W	0.906	0.900	0.881								1.218	1.232	---	1.253	1.260	1.270
Mean RP	OW	0.879	0.875	0.862	0.846	0.832	0.810	0.792	0.840	0.905	1.029	1.070	1.071	1.093	1.141	1.173	1.176
	1W	0.886	0.880	0.867								1.067	1.081	---	1.099	1.122	1.139
Minimum RP	OW	0.880	0.875	0.863	0.847	0.825	0.768	0.690	0.690	0.798	0.865	0.878	0.889	0.861	1.021	1.049	1.041
	1W	0.884	0.876	0.862								0.897	0.939	---	0.983	1.004	1.021
60% N																	
Maximum RP	OW	0.924	0.919	0.924	0.932	0.922	1.038	1.097	1.113	1.149	1.188	1.207	1.223	1.228	1.247	1.253	1.251
	1W	0.930	0.928	0.918								1.175	1.181	---	1.202	1.208	1.211
Mean RP	OW	0.903	0.898	0.891	0.875	0.856	0.834	0.860	0.880	0.828	1.023	1.062	1.077	1.103	1.123	1.134	1.131
	1W	0.908	0.903	0.895								1.055	1.071	---	1.092	1.098	1.102
Minimum RP	OW	0.902	0.896	0.888	0.871	0.835	0.705	0.864	0.885	0.797	0.852	0.875	0.882	0.828	0.974	0.996	1.003
	1W	0.903	0.900	0.891								0.910	0.930	---	0.950	0.970	0.978
50% N																	
Maximum RP	OW	0.948	0.946	0.950	0.952	0.950	1.037	1.083	1.093	1.117	1.144	1.154	1.163	1.165	1.177	1.184	1.179
	1W	0.951	0.948	0.943								1.129	1.134	---	1.147	1.149	1.150
Mean RP	OW	0.929	0.926	0.925	0.921	0.918	0.933	0.942	0.952	0.972	1.023	1.055	1.072	1.086	1.099	1.103	1.099
	1W	0.933	0.929	0.924								1.049	1.063	---	1.080	1.082	1.081
Minimum RP	OW	0.915	0.912	0.903	0.883	0.820	0.744	0.791	0.830	0.869	0.894	0.920	0.937	0.968	0.998	1.011	1.010
	1W	0.918	0.914	0.909								0.953	0.968	---	0.981	0.992	0.996

UNCLASSIFIED

Security Classification

DOCUMENT CONTROL DATA - R & D

(Security classification of title, body of abstract and indexing annotation must be entered when the overall report is classified)

1. ORIGINATING ACTIVITY (Corporate author) Arnold Engineering Development Center ARO, Inc., Operating Contractor Arnold Air Force Station, Tennessee		2a. REPORT SECURITY CLASSIFICATION UNCLASSIFIED	
		2b. GROUP N/A	
3. REPORT TITLE EXPERIMENTAL INVESTIGATION OF TWO BLUNT-TRAILING-EDGE SUPERSONIC COMPRESSOR ROTORS OF DIFFERENT BLADE THICKNESSES AND WITH POLYNOMIAL CAMBER LINE			
4. DESCRIPTIVE NOTES (Type of report and inclusive dates) January - May 1967 - Final Report			
5. AUTHOR(S) (First name, middle initial, last name) C. T. Carman and J. R. Myers, ARO, Inc. and Arthur J. Wennerstrom, Aerospace Research Laboratories, OAR			
6. REPORT DATE January 1969		7a. TOTAL NO. OF PAGES 73	7b. NO. OF REFS 5
8a. CONTRACT OR GRANT NO. F40600-69-C-0001		9a. ORIGINATOR'S REPORT NUMBER(S) AEDC-TR-68-251	
b. PROJECT NO.		9b. OTHER REPORT NO(S) (Any other numbers that may be assigned this report) N/A	
c. Program Element 614450F			
d.			
10. DISTRIBUTION STATEMENT This document has been approved for public release and sale; its distribution is unlimited.			
11. SUPPLEMENTARY NOTES Available in DDC		12. SPONSORING MILITARY ACTIVITY Arnold Engineering Development Center, Air Force Systems Command, Arnold Air Force Station, Tennessee	
13. ABSTRACT Two configurations of blunt-trailing-edge supersonic compressor blades incorporating a polynomial camber line were tested with air in the AEDC compressor rig. The performance of these blades was investigated over the speed range from 50 to 100 percent of design speed. The performance at the two blade configurations is compared, and the effect of the modifications between the two configurations is evaluated. A comparison of selected performance data obtained with circular arc blading tested previously and the polynomial camber blading is made to evaluate the effects of the camber redistribution.			

14

KEY WORDS

LINK A

LINK B

LINK C

ROLE

WT

ROLE

WT

ROLE

WT

1 axial-flow compressors -- - *Performance*

2 compressor blades -- "

3 trailing edges

blunt bodies

camber

performance

pressure distribution

4. Blades -- *Performance*

1-2